Earth and Space Science

RESEARCH ARTICLE
10.1029/2024EA003902

Key Points:

- Flash heavy rain events (FHREs) are most frequent during Meiyu, increasing from northwest to southeast across the middle Yangtze River basin
- Before FHREs, strong southerlies dominate the lower troposphere in the east, while weak easterlies prevail in the west
- Hours before rainfall, winds accelerate notably over the eastern plain, while directional shifts are observed over the western mountains

Correspondence to:
X. Wang,
wxk816@163.com

Citation:
Wang, J., Wang, X., Yuan, H., Cui, C., Wang, X., & Liu, L. (2025). Wind profile characteristics that warn of summertime flash heavy rain events over the middle reaches of the Yangtze River basin. *Earth and Space Science*, *12*, e2024EA003902. https://doi.org/10.1029/2024EA003902

Received 31 JUL 2024
Accepted 27 JAN 2025

Author Contributions:
Conceptualization: Jingyu Wang, Xiaokang Wang
Data curation: Xiaofang Wang
Formal analysis: Huiling Yuan
Investigation: Huiling Yuan
Methodology: Xiaokang Wang, Huiling Yuan
Resources: Chunguang Cui
Supervision: Huiling Yuan, Chunguang Cui
Writing – original draft: Jingyu Wang, Xiaokang Wang
Writing – review & editing: Lin Liu

Wind Profile Characteristics That Warn of Summertime Flash Heavy Rain Events Over the Middle Reaches of the Yangtze River Basin

Jingyu Wang[1,2], Xiaokang Wang[1], Huiling Yuan[2], Chunguang Cui[1], Xiaofang Wang[1], and Lin Liu[1]

[1]China Meteorological Administration Basin Heavy Rainfall Key Laboratory/Heavy Rainfall Research Center of China/Hubei Key Laboratory for Heavy Rain Monitoring and Warning Research, Institute of Heavy Rain, China Meteorological Administration (CMA), Wuhan, China, [2]School of Atmospheric Sciences and Key Laboratory of Mesoscale Severe Weather/Ministry of Education, Nanjing University, Nanjing, China

Abstract Forecasting and early warnings for summertime flash heavy rain events (FHREs) in the middle Yangtze River basin (MYRB) pose significant challenges. This study examined variations in lower tropospheric wind profiles hours before these FHREs using reanalysis data and wind profile radar observations. The findings highlight wind accelerations, directional shifts, and associated vertical shears preceding FHREs, providing valuable insight for severe weather warnings. During the summers of 2010–2019, FHREs occurred most frequently and contributed significantly to total precipitation during the Meiyu period, compared to before and after. Meiyu FHREs also exhibit longer durations and nocturnal peaks. Spatially, FHRE frequency increases from northwest to southeast, with higher frequencies in the topographic areas. The discernible moisture influx 4 hr before FHREs primarily comes from southwesterly and easterly winds below 700 hPa. Before FHRE, weaker easterly winds dominated western MYRB, while strong southerly winds prevailed in the east, influenced by mesoscale cyclonic shear and low-level jets. Detailed wind changes below 4 km altitude show that over the southeastern MYRB, accelerated west-southwest winds are observed 3–4 hr before FHREs, while southerly components near the boundary layer top intensified 2 hr earlier. Within 1 hr before FHREs, the wind speeds sharply increase to peak. East of the western mountains, southwesterly winds strengthen 5 hr prior, then weaken as they shift to northerlies just before FHREs, accompanied by reinforced northerlies near the surface. Over the western mountainous area, southeasterly components below 2 km altitude increase 4 hr before FHREs, although at lower speeds.

1. Introduction

Flash heavy rain, defined as hourly accumulated rainfall of ≥20 mm or ≥50 mm over 3 hr, significantly contributes to summertime flash flooding in China (X. Yu, 2013). The small scale, abrupt occurrence, and intensity of such rainfall pose challenges for accurate forecasting and timely warnings (Brooks & Stensrud, 2000). Recent studies about catastrophic extreme rainfall events in eastern China have highlighted the complex mechanism underlying their formation and exposed the limitations of numerical models in accurately forecasting such abrupt heavy rain. For instance, during the unprecedented rainfall on 21 July 2012, in Beijing, hourly precipitation reached a record-breaking 85 mm (Zhang et al., 2013). Similarly, on 20 July 2021, at 17:00 Beijing time, the Zhengzhou station in Henan Province recorded an hourly rainfall of 201.9 mm, far exceeding historical July precipitation averages for Henan (Zhang et al., 2023). Studies indicate that flash heavy rain often occurs within episodes of heavy rainfall events (Wang et al., 2019; X. Yu, 2013), which can be directly caused by typhoons, mesoscale shear lines, vortices, surface fronts, or even weak synoptic forcing conditions (Luo et al., 2016). These heavy rainfall events, closely associated with the northward-advancing summer monsoon, exhibit significant intra-seasonal distinctions (S. Tao, 1980).

The middle reaches of the Yangtze River basin (MYRB), primarily situated in Hubei Province with China's secondary-step terrain to the west, is prone to frequent and intense precipitation events, including occasional extreme FHREs (Zhang & Zhai, 2011). These regional catastrophic events are caused by the mesoscale weather systems, including shear lines, vortices, and Meiyu fronts. Additionally, they are influenced by low-level jets from the southwest or east (Cui et al., 2023), as well as multiscale weather systems originating from the Tibetan Plateau and moving eastward (Tao & Ding, 1981). Given the recent advancements in surface observations, there is a need for in-depth research into the mechanisms, forecasting, and warning of the flash heavy rain in the MYRB.

In various synoptic and mesoscale situations, favorable conditions such as thermodynamic structure, atmospheric destabilization, wind pattern, precipitable water vapor, and upward vertical motion are essential for the occurrence of FHREs (Doswell et al., 1996). Therefore, it is necessary to clarify the impact of wind vectors. Before the onset of intense precipitation, winds play a crucial role in inducing vertical perturbations, dynamic instabilities like symmetric and shear instabilities, as well as in transporting abundant water vapor and potential energy (Markowski & Richardson, 2011; Wang, Zhou, et al., 2022). Du and Chen (2019) indicated that mesoscale updrafts, resulting from convergence in the exit region of the boundary-layer jet and divergence in the entrance region of the synoptic low-level jet, can initiate convective systems directly responsible for heavy precipitation along the South China coast. Xue et al. (2018) demonstrated that boundary-layer jets due to the inertial oscillations are critical to nocturnal heavy rain associated with the Meiyu front in the MYRB. Additionally, 39.1% of extreme hourly rainfall records in China are closely associated with cyclonic circulations attributed to mesoscale vortices or shear lines (Huang et al., 2024; Luo et al., 2016). Particularly in central China, mesoscale vortices or shear lines occur frequently due to eastward-moving southwest vortices (Fu et al., 2022), and the blocking and deflecting effects of China's secondary-step terrain. Moreover, lower tropospheric vertical shear also plays an important role in initiating new cells and organizing convective systems that directly lead to extreme flash heavy rain in eastern China (Zheng et al., 2013). Therefore, the key factors before precipitation, including low-level jets, mesoscale cyclonic circulation, and vertical shear, could lay the foundation for early warning systems for FHREs.

Preceding severe weather, changes in winds can be detected using high-resolution observations from a wind profile radar (WPR) (Benjamin et al., 2004; May & Wilczak, 1993; Strauch et al., 1987; Weber et al., 1990). Continuous wind profiles are conducive to forecasting severe weather by revealing wind perturbations resulting from the movement and development of mesoscale or synoptic-scale systems in advance (Coleman & Knupp, 2011; Guo et al., 2023; Larsen & Röttger, 1982; Neiman et al., 1992; Shapiro et al., 1984). Forecasting flash heavy rain in the MYRB is challenging because of the complex interactions among factors such as topography, upstream weather systems, and boundary layer oscillation. Although some case studies have explored the use of WPR observations in severe weather warnings (Cui et al., 2011; Gao et al., 2021; Sun et al., 2005), there is a gap in analyzing the statistical characteristics of wind profiles that are effective for warning of FHREs over the MYRB. Therefore, this study uses several years of WPR data from specific stations in the MYRB to examine the detailed changes and corresponding timing of winds before flash heavy rain. The findings aim to deepen our understanding of the underlying mechanism and enhance the accuracy of flash heavy rain warnings.

2. Data and Methodology

Because Hubei Province covers most of the middle reaches of the Yangtze River basin (MYRB) (Figure 1a), it is chosen as the study area (Figure 1b). The regional topography, extracted from the global ETOPO1 (i.e., "Earth TOPOgraphy" at the resolution of one arcminute) data set produced by the U.S. National Oceanic and Atmospheric Administration, is shown in Figure 1.

Based on hourly observations of approximately 2618 surface rain gauges, the detailed statistical features of flash heavy rainfall in MYRB during the summers (June–August) of 2010–2019 are analyzed. New surface automatic weather stations (AWSs) have steadily been deployed over the past 10 years (Leng et al., 2021). The expanded rain gauge network impacts the annual frequency of rainfall. Consequently, this study overlooks the annual variation of summertime flash heavy rainfall and focuses more on its intra-seasonal variations.

As flash heavy rain often occurs within continuous heavy rainfall events, this study primarily focuses on FHREs. Each FHRE at AWS was defined as accumulative 3-hr rainfall of ≥30 mm, with at least ≥20 mm of rainfall in 1 hr (Chen et al., 2021; Wang et al., 2019). The duration of an FHRE is calculated from the period when the hourly rainfall amount exceeds 5 mm from start to finish.

The study utilized ERA5 data, a fifth-generation reanalysis from the European Center for Medium-Range Weather Forecasts, spanning the summers of 2010–2019. This data set provides spatial depictions of horizontal prevailing winds in the lower troposphere, with the profiles of water vapor flux and wind patterns preceding FHREs. It operates at a resolution of $0.25° \times 0.25°$ and includes 37 pressure levels, with a temporal resolution of

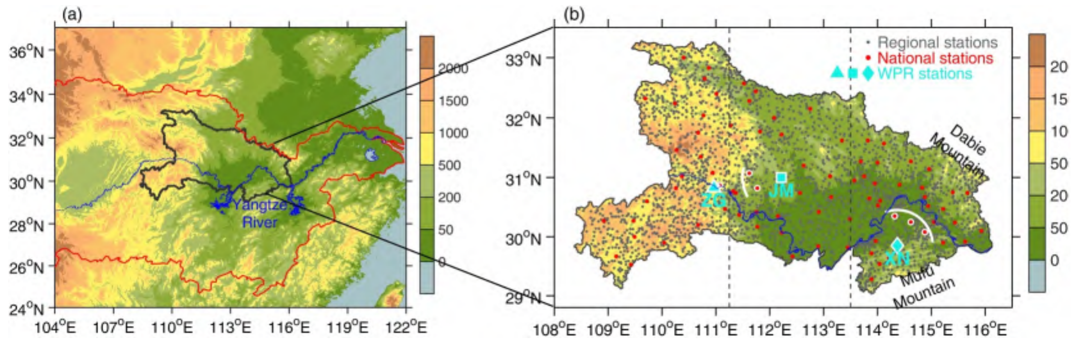

Figure 1. (a) Topography (shading, unit: m) of eastern China. The blue line shows the course of the Yangtze River, red line delineates the Yangtze River basin. (b) Topography (shading, unit: m) and distribution of surface automatic weather stations (AWSs) in the middle Yangtze River basin. Red dots represent the national surface AWSs, and gray dots indicate the regional surface AWSs. The closed cyan diamond, square, and triangle denote the stations with wind profile radar (WPR, XN: Xianning, JM: Jingmen, and ZG: Zigui). White arcs delineate the 85-km downstream range of WPRs. Stations outlined in white are leeward national sites within the impact range of WPRs. Three areas, divided by two gray dash lines, are utilized for the spatial averaging of winds in Figure 10.

1 hr, precisely matching the start time of FHREs. The data are also employed to quantify wind spread between the reanalysis and the WPR data before FHREs.

Five AWSs (i.e., Xianning, Jingmen, Zigui, Hankou, and Xiantao) in the MYRB have been equipped with WPRs to observe three-dimensional winds continuously. Wind profile data collected every 6 min at these stations during the summers of 2015–2018 (Xianning: 2015–2019) is included, encompassing horizontal wind speed and direction, vertical wind, refractive index structure parameter, and quality control indexes of the horizontal and vertical winds. Vertical observations extend to approximately 9–11 km above ground level (AGL). The vertical intervals are 60 m below 0.82 km AGL, 120 m between 0.94 and 2.02 km, and 240 m above 2.26 km at all stations except Xianning, which has intervals of 120 m below 1.95 km, 240 m between 2 and 3.92 km, and 480 m above 4 km.

Three of the five WPR stations are chosen for this study at Xianning (XN), Jingmen (JM), and Zigui (ZG) (Figure 1b), based on their continuous records during the 12 hr preceding the associated FHREs. Previous studies have demonstrated that hourly WPR horizontal winds over the lower reaches of the Yangtze River basin are consistent with ERA5 winds, showing correlation coefficients exceeding 0.76 and standard deviations below 3.26 m s^{-1} (Deng et al., 2022). Then, the hourly WPR winds, averaged over the 6-min observations, within 12 hr before the 38 FHREs in the MYRB are validated against ERA5 hourly horizontal winds using bias and root-mean-square error (RMSE). They are defined as

$$\text{bias} = \frac{1}{N}\sum\left|w_i^k - e_i^k\right|, \tag{1}$$

and

$$\text{RMSE} = \left[\frac{1}{N}\sum\left|w_i^k - e_i^k\right|^2\right]^{1/2}, \tag{2}$$

with WPR and ERA5 hourly winds w_i^k and e_i^k, respectively, at the same hour i and height k; N is the sum number of hours and heights; the less one between $\left|w_i^k - e_i^k\right|$ and $360 - \left|w_i^k - e_i^k\right|$ is taken when calculating the bias and RMSE of the wind direction.

The comparison (Table 1) reveals that the absolute biases for wind speed and direction at altitudes below 5 km AGL are relatively small, with biases of 1–2 m s^{-1} for speed and less than 46° for direction. The RMSEs are approximately 2 m s^{-1} for speed and 44–65° for direction, which are comparable to the standard deviation of WPR observations (Wuertz et al., 1988). Notably, wind biases and RMSEs in the 0–2 km layer surpass those in the 2–5 km layer, owing to the finer vertical intervals. Moreover, the significant wind direction biases and RMSEs

Table 1
Absolute Biases and Root-Mean-Square Errors (RMES) Between the ERA5 and Wind Profile Radar Horizontal Winds at Stations XN, JM, and ZG Within 12 hr Before Flash Heavy Rain Events

		Wind speed (m s^{-1})		Wind direction (°)	
Station	AGL (km)	Bias	RMSE	Bias	RMSE
XN	0–5	2.05	2.65	35.30	53.46
	0–2	1.99	2.65	38.85	56.8
	2–5	2.12	2.64	27.69	45.12
JM	0–5	2.18	3.13	27.83	44.79
	0–2	2.12	2.86	33.33	51.79
	2–5	2.18	3.41	18.01	27.87
ZG	0–5	1.58	2.04	46.01	62.43
	0–2	1.69	2.16	58.2	73.78
	2–5	1.37	1.79	28.59	41.46

at station ZG in the 0–2 km layer, when compared to other stations, are primarily attributed to the local terrain effects. Overall, WPR observations obtained at these three stations, with a vertical resolution of 60–480 m, can effectively characterize the low-level wind profile features, and enable more detailed quantitative statistical analyses.

The wind consistency at given hours before FHREs across different cases was calculated as the ratio of the vector mean and arithmetic average wind speeds, as follows (Stewart et al., 2002; Zhong et al., 2004):

$$C_j^z = \sqrt{\left(\frac{1}{N}\sum_{i=1}^{N} u_i\right)^2 + \left(\frac{1}{N}\sum_{i=1}^{N} v_i\right)^2} \Bigg/ \frac{1}{N}\sum_{i=1}^{N}\sqrt{u_i^2 + v_i^2}, \tag{3}$$

where C_j^z denotes wind consistency at the j^{th} hour before FHREs at a height of z at one site, and N is the number of FHRE cases associated with this WPR site. The consistency values range from 0 to 1. A consistency value of 1 indicates that the winds blow from the same direction at a given hour before all FHRE cases, while a consistency value of 0 indicates that winds blow from all directions or are equally split between opposite directions.

Boxplots are used in this study to depict the spread and skewness of FHREs and wind speeds before FHREs. On each box, the central mark (circle or line) represents the median (q_2), while the bottom and top edges of the box indicate the 25th (q_1) and 75th (q_3) percentiles, respectively. Additionally, the mean value is depicted by a dot. The lower and upper whiskers extend to the non-outlier extreme data points. Outliers (Grubbs, 1969) are individually plotted as a "+" symbol if they exceed $q_3 + 1.5 \times (q_3\text{-}q_1)$ or fall below $q_1\text{-}1.5 \times (q_3\text{-}q_1)$.

3. Results

3.1. Temporal and Spatial Distribution of FHREs in Summer

The dates of the pre-Meiyu, Meiyu, and post-Meiyu periods in the MYRB during the summers of 2010–2019 are depicted in Figure 2a. Post-Meiyu days dominate, comprising 51% of summer days, while pre-Meiyu days are the fewest. The Meiyu period typically spans from mid-June to early July, lasting 13–35 days, and constitutes 29% of summertime (Figures 2a and 2b). However, during the Meiyu period, both rainfall amount and accumulated precipitation of FHREs peak. Additionally, the proportion of FHRE precipitation is highest during the Meiyu period, contributing 21.6% (Figure 2b). It is worth noting that the precipitation intensity of FHREs, calculated as the rainfall amount divided by the frequency, remains consistent across all three summer periods. However, Meiyu FHREs contribute 54% of the total summer FHRE rainfall amount. This substantial contribution is mainly due to their high frequency, accounting for 50% of all FHRE occurrences in summer (Figure 2c).

The duration boxplot (Figure 2c) shows that most FHREs during the pre-Meiyu and post-Meiyu periods last less than 4 hr. In contrast, those occurring in the Meiyu period have a maximum duration of 24 hr, with the majority lasting less than 7 hr. FHREs with longer durations are more prevalent during the Meiyu period. The median and 75th percentile of FHRE duration during this period are 1 hr longer than in the other two periods. Half of the Meiyu FHREs last for more than 3 hr, in contrast to only 25% of FHREs in the other periods. The durations of pre-Meiyu FHREs are skewed toward a longer range compared to the post-Meiyu ones. This results from the larger mean duration of pre-Meiyu FHREs, despite the median, 25th percentile, and 75th percentile being the same for both.

The normalized diurnal frequency (Yu et al., 2007) of FHREs over the MYRB is depicted in Figure 2d. Summer FHREs occur more frequently from 15:00 to 00:00 BJT (Beijing Time), peaking at 17:00. During the pre-Meiyu and post-Meiyu periods, the FHREs also peak at 17:00, contributing to the afternoon peak in summer. However, pre-Meiyu FHRE frequency exhibits secondary peaks in the midday and midnight, unlike the post-Meiyu one, which only has a single afternoon peak. During the Meiyu period, FHREs show a notable nocturnal pattern, occurring more frequently from 02:00 to 10:00, with a peak at 06:00. The nocturnal boundary layer jet resulting from inertial oscillation (Xue et al., 2018) may be a dominant factor facilitating FHREs at night, in addition to the

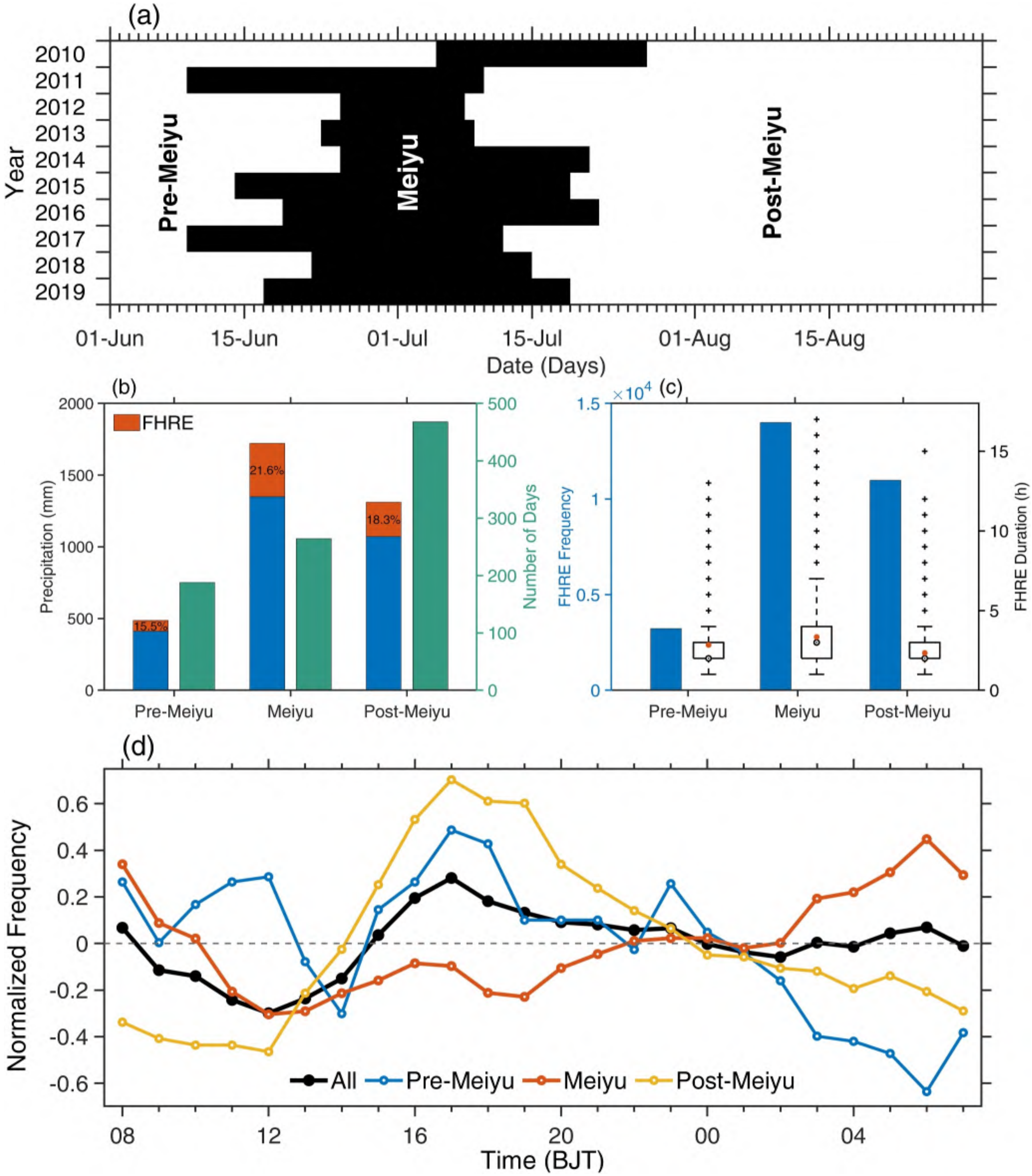

Figure 2. (a) Dates of pre-Meiyu, Meiyu, and post-Meiyu periods during the summers of 2010–2019. (b) Number of days (green bars) and accumulated precipitation (blue bars, unit: mm) during three periods. (c) Frequency (blue bars) and duration of flash heavy rain events (FHREs) (boxplots: black circles show the median and red dots show the mean, unit: h) during the three periods. (d) Diurnal normalized frequency of FHREs.

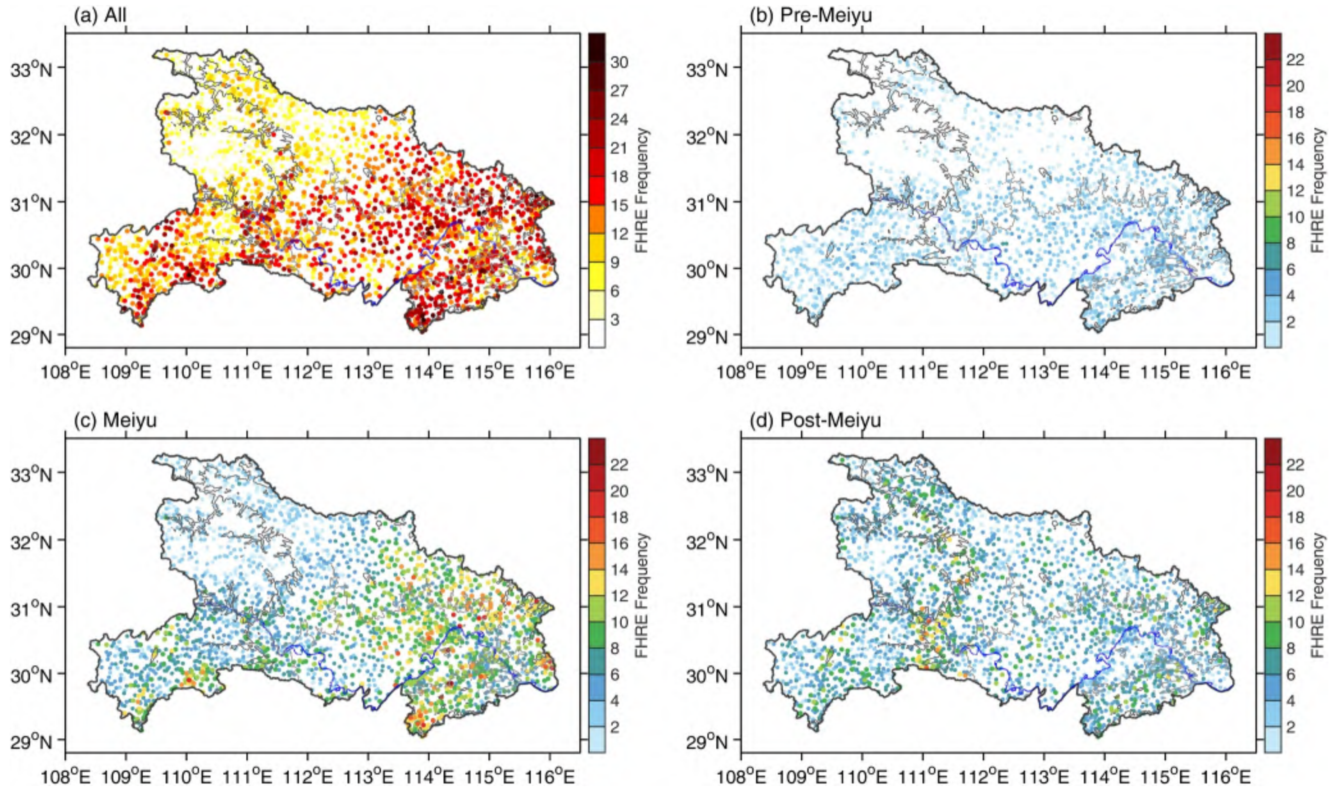

Figure 3. Spatial distribution of flash heavy rain event (FHRE) frequency during summers of 2010–2019, (a) all FHREs, (b–d) FHREs occurring during the pre-Meiyu, Meiyu, and post-Meiyu periods, respectively. The blue line denotes the course of the Yangtze River. The light (dark) gray lines indicate terrain at 50 (500) m elevation.

synoptic system and mountain-plain solenoid (Sun & Zhang, 2012). Moreover, the Meiyu FHREs show the smallest diurnal frequency amplitude, while the post-Meiyu ones demonstrate the largest amplitude.

The spatial distribution of summer FHREs (Figure 3) shows an increasing frequency from the northwest to the southeast. Particularly, high FHRE frequency is observed near mountainous areas, such as the eastern MYRB near the Dabie Mountains and Mufu Mountains, as well as the west mountain front south of 31.5°N (Figure 3a). Stations exhibit higher FHRE frequency during the Meiyu period compared to other periods. In the pre-Meiyu period (Figure 3b), FHREs are more prevalent in the area south of 31°N, with little disparity in frequency between east and west. During the Meiyu period (Figure 3c), FHRE frequency varies unevenly across different stations. Notably high frequency is observed at stations east of 113°E and in the southwest corner, especially along the southern slope of the Dabie Mountains, the northern foothills of the Mufu Mountains, and the eastern margin of the central plain. By the post-Meiyu period (Figure 3d), FHRE frequency is more evenly distributed in space, even increasing in the northwest area, which previously had low FHRE frequency in the pre-Meiyu and Meiyu periods. Furthermore, some stations along the western mountain fronts above 500 m elevation exhibit more frequent occurrences. In summary, the spatial distributions of FHREs in the three periods suggest a combined influence of the northward monsoon and complex mesoscale terrain on heavy precipitation across the MYRB in summertime (Hu et al., 2001; S. Tao, 1980; Yang et al., 2020).

3.2. Synoptic Patterns in Summer and Prevailing Winds Before the FHREs

In summer (Figure 4a), the northwestern outer edge of the subtropical high, marked by a geopotential height of 5,860 gpm at 500 hPa, extends to the Yangtze River in the mid-troposphere. Lower tropospheric southwesterly winds facilitate the northward transport of warm and moist air from lower latitudes, promoting precipitation in the MYRB. However, significant variations in synoptic patterns are observed across the three periods.

During the pre-Meiyu period (Figure 4b), the westerly winds caused by the straight geopotential heights impact the mid-troposphere of the MYRB, due to the positioning of the subtropical high at lower latitudes. Low-level

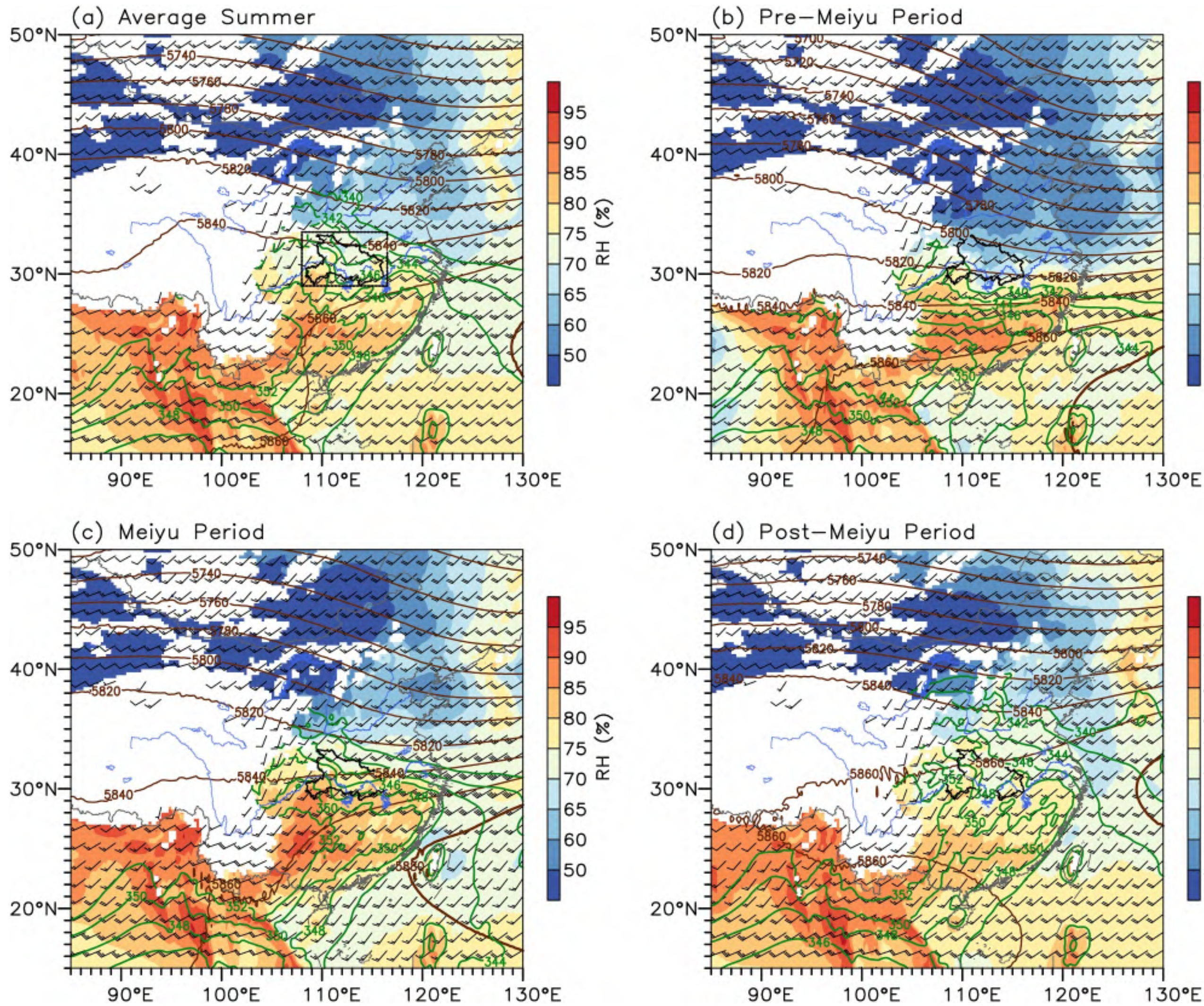

Figure 4. Average synoptic patterns during the (a) summers, (b) pre-Meiyu, (c) Meiyu, and (d) post-Meiyu periods of 2010–2019. The brown contours show the geopotential height at 500 hPa (unit: gpm), green contours show the equivalent potential temperature (θ_e) at 850 hPa (unit: K), shadings show the relative humidity at 850 hPa (unit: %), and barbs represent the vector winds at 700 hPa (unit: m s^{-1}, full and half barbs denote 4 and 2 m s^{-1}, respectively). The blanks indicate terrain-blocked areas. The black dashed box in panel (a) shows the four boundaries for calculating the water vapor flux in Figure 5.

westerly winds are relatively weak over the MYRB but become strong south of 30°N. The leading edge of the monsoon, indicated by the equivalent potential temperature (θ_e) of 340 K at 850 hPa, extends south of the Yangtze River, with low-level relative humidity below 60% over the MYRB.

During the Meiyu period (Figure 4c), most areas of the MYRB are covered by the northwestern outer margin of subtropical high as it migrates northward. Low-level winds strengthen, particularly with a pronounced southerly component compared to the pre-Meiyu period, causing the leading edge of the monsoon to cross the study area. The Meiyu front, characterized by the great gradient of θ_e at 850 hPa, covers the MYRB. These intensified winds and quasi-stationary font provide abundant water vapor, potential energy, and symmetric instability conducive to heavy rainfall (S. Tao, 1980; Wang, Zhou, et al., 2022).

By the post-Meiyu period (Figure 4d), the western periphery of subtropical high extends over eastern China south of the Yangtze River as it continues to move northward. The low-level winds, which have become more southerly, are weaker than the Meiyu period. Relative humidity remains comparable to that during the Meiyu period, even though the leading edge of the monsoon advances to 40°N. Overall, the distinctions in synoptic patterns across these three periods highlight the crucial role of lower tropospheric winds and moisture in influencing heavy rain.

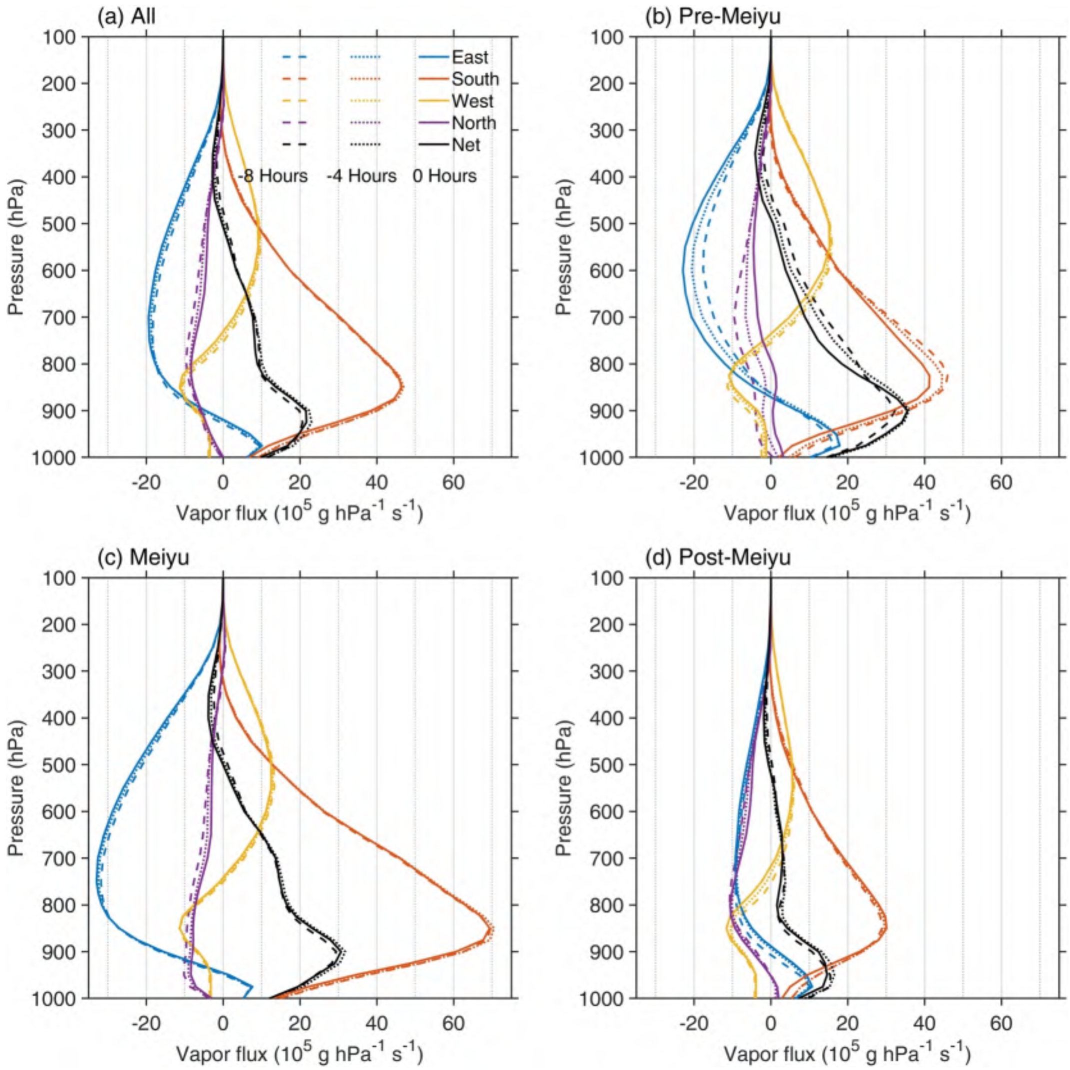

Figure 5. Vertical profiles of water vapor flux along the four boundaries of middle Yangtze River basin (as shown in Figure 4a) at the 0, 4, and 8 hr before the start of flash heavy rain events during the (a) summer and (b–d) three periods of 2010–2019. The positive (negative) values show the water vapor influx (outflux).

Figure 5 illustrates the water vapor flux over the MYRB resulting from prevailing winds at 0, 4, and 8 hr before the start of FHREs. In summer (Figure 5a), positive net water vapor fluxes, known as moisture convergence, primarily occur below 500 hPa. Moisture inflows predominantly come from the southern boundary across all vertical levels, the eastern boundary below 900 hPa, and the western boundary above 700 hPa. Moisture convergence 8 hr before FHREs is slightly smaller than the start hours but becomes greater 4 hr before, especially below 800 hPa.

The differences in water vapor flux before FHREs are generally minimal across various hours, except during the pre-Meiyu period (Figure 5). However, distinctions among the three periods are evident. During the pre-Meiyu period (Figure 5b), most water vapor below 750 hPa comes from the southern and eastern boundaries. As FHREs approach, there is a noticeable increase in moisture from the northern boundary, highlighting significant cold air influx from the north. Moving into the Meiyu period (Figure 5c), the peak water vapor flux from the southern boundary remains the highest among the three periods. However, the net flux at 900 hPa is similar to the pre-Meiyu period due to increased outflow from the eastern boundary. Furthermore, vertically integrated moisture convergences before Meiyu FHREs (Figure 5c), indicated by the integral area between the positive net flux and zero, show the strongest intensity, owing to a secondary peak at 700 hPa. This deeper convergence layer of moisture during the Meiyu period facilitates a higher frequency of FHREs (Figure 2c). After the Meiyu period (Figure 5d), moisture convergence weakens as winds from all directions decrease. Therefore, understanding the lower-tropospheric prevailing wind patterns before FHREs is essential.

In addition to the northward-advancing summer monsoon, the mesoscale mountains across the MYRB also influence the prevailing wind patterns. Hence, the prevailing wind profiles before FHREs averaged over the western, central, and eastern areas of the MYRB (Figure 1b), are depicted in Figure 6. In summer (Figures 6a1–6a3), variations in horizontal winds occur below 500 hPa, characterized by a shift from easterlies to westerlies with a clockwise rotation with height. Wind speeds increase from west to east, coinciding with a reduction in the clockwise rotation. Across the three periods, horizontal wind speeds peak in the pre-Meiyu period, except in the eastern area during the Meiyu period (Figure 6c3). As FHREs approach, low-level easterly winds deepen over the western area, while wind speeds below 900 hPa (at 850–700 hPa) notably increase over the central (eastern) area.

Over the western mountainous area (Figures 6b1–6d1), there is a noticeable clockwise wind rotation with height as FHREs approach across the summer, with minimal variations in wind speed. Conversely, over the eastern area (Figures 6b3–6d3), wind speeds below 500 hPa peak during the Meiyu period, exhibiting a slight increase 8 hr before FHREs at 850 hPa (Figure 6c3), compared to the other periods. The wind speeds increase 4 hr before the pre-Meiyu FHREs at 925 hPa, followed by the rise 2 hr before at 700 hPa (Figure 6b3). The wind speeds increase 4 hr before the post-Meiyu FHREs at 700 hPa (Figure 6d3). The variations in low-level winds preceding FHREs over the central area (Figures 6b2–6d2) differ across the three periods, contrasting with the other two areas. A slight increase in wind speed at 925 hPa is evident during the Meiyu period (Figure 6c2), while more pronounced clockwise wind rotation occurs in the other two periods (Figures 6b2 and 6d2).

Based on reanalysis data, qualitative changes in synoptic-scale prevailing winds can be observed before FHREs, including intensified southwesterly winds and clockwise rotation, although the specific lead hours remain to be further determined.

The spatial distributions of horizontal winds indicate that synoptic low-level jets (Figures 7a1 and 7a2) (Du et al., 2014), boundary-layer jets (Figure 7a3) (Xue et al., 2018), and mesoscale cyclonic wind shear (Figures 7a2–7a4) (Feng et al., 2016) are the primary systems influencing the summer FHREs in the MYRB. These systems begin to significantly intensify 4 hr before reaching their peak for FHRE onset (Figures 7b1–7b4 and 7a1–7a4). The impact areas of these systems vary across the three periods, with notable distinctions between 0 and 4 hr before the FHREs just in the pre-Meiyu period (Figures 7 and 8).

During the pre-Meiyu period, strong southwesterly and southerly winds are prevalent to the south of the MYRB (Figures 7d1–7d4), and the onset of FHREs is closely associated with their northward surge (Figures 7c1–7c4). Southwesterly winds dominate the MYRB at 700 hPa as FHREs start, with wind speeds increasing from northwest to southeast (Figure 7c1). Cyclonic wind shear contributes to the gradual extension of easterly winds across the MYRB from 850 hPa to the surface (Figures 7c2–7c4). When the FHREs start, southerly winds (Figures 7c2–7c4) primarily affect the eastern area of the MYRB due to frequent low-level and boundary-layer jets. On the other hand, the central and western areas are mainly impacted by deep easterlies (Figures 6b1–6b2). These winds are primarily caused by cyclonic wind shear resulting from the deflection and deceleration of the southerly flows by the western mountains, which range from 500 to 2,000 m in elevation (Figure 1b). Below 850 hPa, easterlies over central areas are particularly robust due to the boundary layer jets without blocking from the Mufu Mountains.

The low-level horizontal prevailing winds show minimal variation between 4 and 0 hr before the FHRE during both the Meiyu and post-Meiyu periods (Figure 8). This suggests that the smaller-scale weather systems or thermodynamic feedbacks have a more significant impact on flash heavy rain (Luo et al., 2016; Wang, Zhou, et al., 2022), overshadowing the influence of synoptic-scale flows. During the Meiyu period (Figures 8a1–8a3 and 8b1–8b3), the greatest zonal gradients of wind speed are observed near the central MYRB. The study area is characterized by weak easterlies in the western MYRB, transitioning to strong southerlies over the central and eastern MYRB. This pattern arises from the frequent presence of synoptic low-level jets and approaching boundary-layer jets from the south (Du et al., 2014), combined with northward-moving cyclonic wind shear associated with the monsoon's progression northward (Figure 4c). In the post-Meiyu period (Figures 8c2–8c4 and 8d2–8d4), wind speeds decrease over the MYRB. However, higher wind speeds below 700 hPa continue in the central area due to boundary-layer jets.

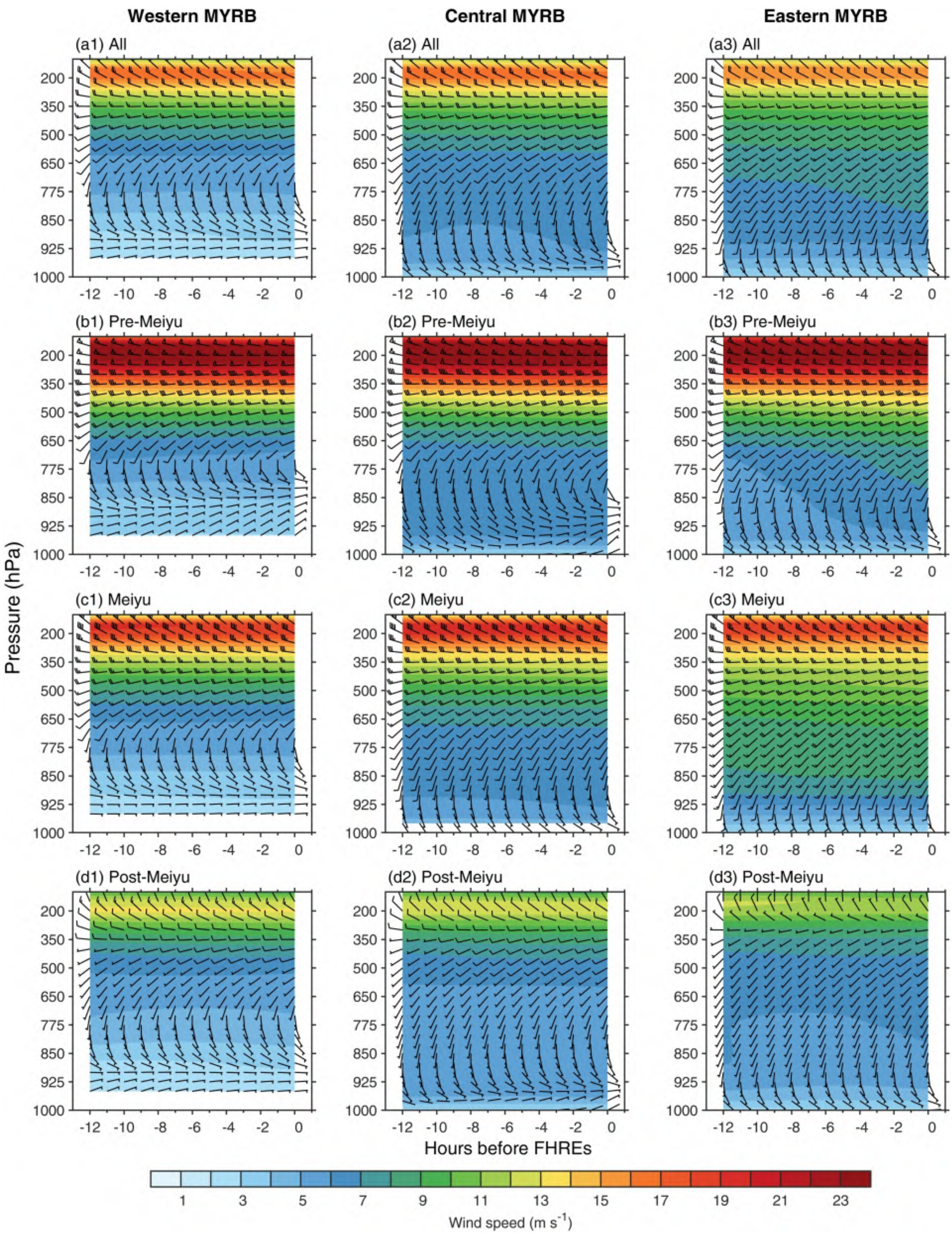

Figure 6. Wind profiles averaged over distinct areas of middle Yangtze River basin (Figure 1b) within 12 hr before flash heavy rain events during the (a1–a3) summer, (b1–b3) pre-Meiyu, (c1–c3) Meiyu, and (d1–d3) post-Meiyu periods of 2010–2019. The half barb, full barb, and pennant symbols denote averaged vector winds with speeds of 2, 4, and 20 m s^{-1}, respectively. Shading indicates the averaged wind speeds.

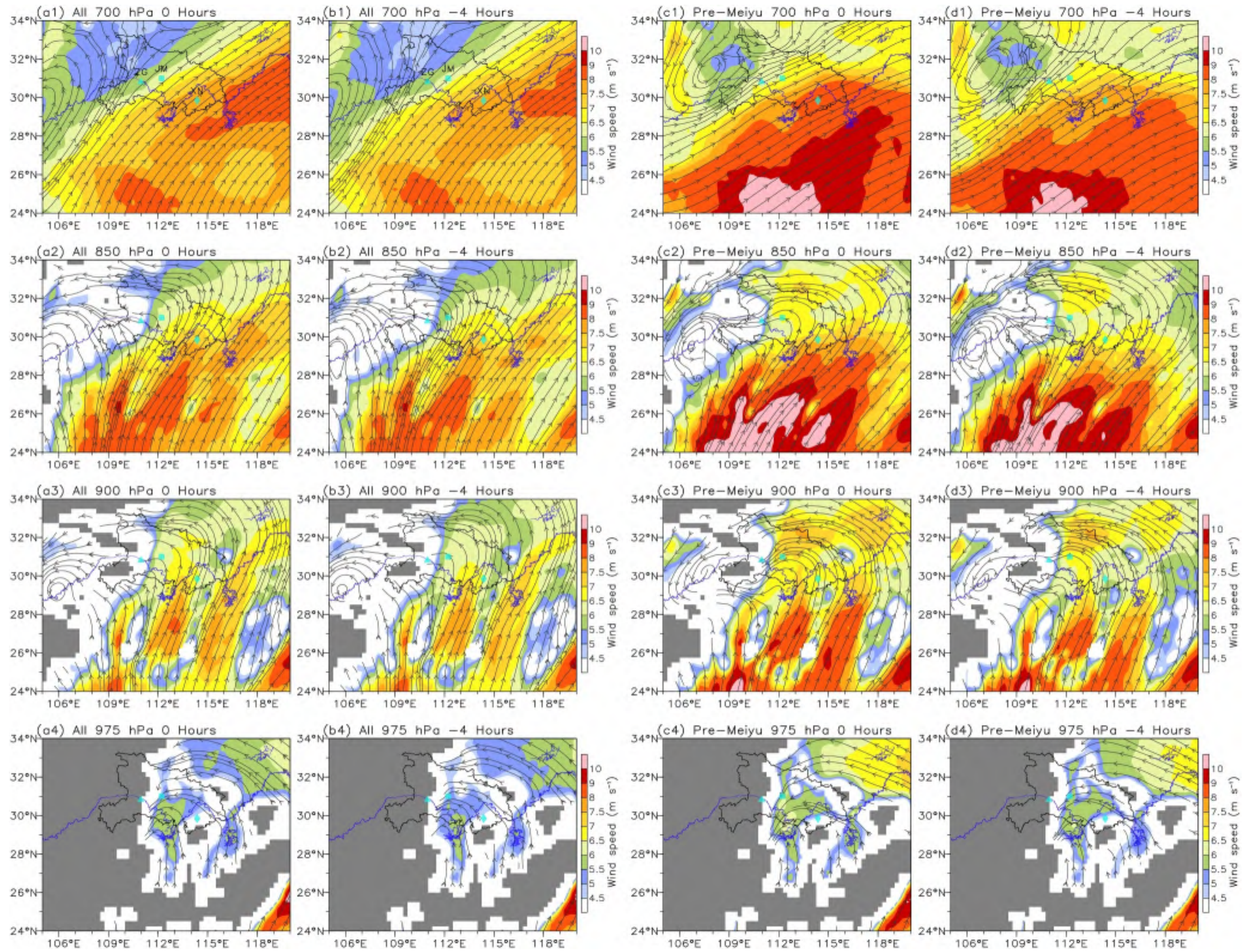

Figure 7. Averaged horizontal flow (gray streamlines) and wind speed (shading, unit: m s^{-1}) at 0 hr before the start of flash heavy rain events (FHREs) during the summers and pre-Meiyu periods of 2010–2019 over the middle Yangtze River basin are depicted in panels (a1–a4, c1–c4) at 700, 850, 900 and 975 hPa. Panels (b1–b4, d1–d4) show the same parameters at 4 hr before FHREs onset. Gray shadings indicate terrain-blocked areas. The closed cyan diamond, square, and triangle denote the wind profile radar sites. The blue line represents the Yangtze River.

3.3. Detailed Wind Profile Characteristics Indicative of FHREs

As previously noted, reanalysis data reveals discernible variations in the lower-tropospheric winds preceding FHREs during the pre-Meiyu periods, as opposed to those during the Meiyu or post-Meiyu periods (see Figures 6–8). Therefore, detailed wind changes before FHRE onset can be thoroughly investigated using the WPR data, which provides denser vertical intervals.

When summer FHREs start, station XN is primarily influenced by strong southerly winds below 700 hPa, while stations JM and ZG experience weaker easterly winds (Figures 7a2–7a4). Consequently, 4–6 leeward surface rain gauges, including those equipped with WPR (i.e., surface AWSs with white outlines in Figure 1b), were selected to obtain the associated FHREs. Subsequently, FHREs that began at different hours within the same rainfall event were merged. The start times of FHREs were also refined by considering the WPR vertical velocity $\geq +2$ m s^{-1}, indicating the presence of falling precipitation particles (Garcia-Benadi et al., 2022; Wuertz et al., 1988). Ultimately, 38 FHREs (XN: 15, JM: 9, and ZG: 14) with available 6-min WPR observations were manually identified.

Using wind roses at three sites 1 hr before the start of the FHREs (Figure 9), the quantitative contribution of favorable wind vectors to FHREs and spatial distinction in horizontal winds just before the FHREs are detailed

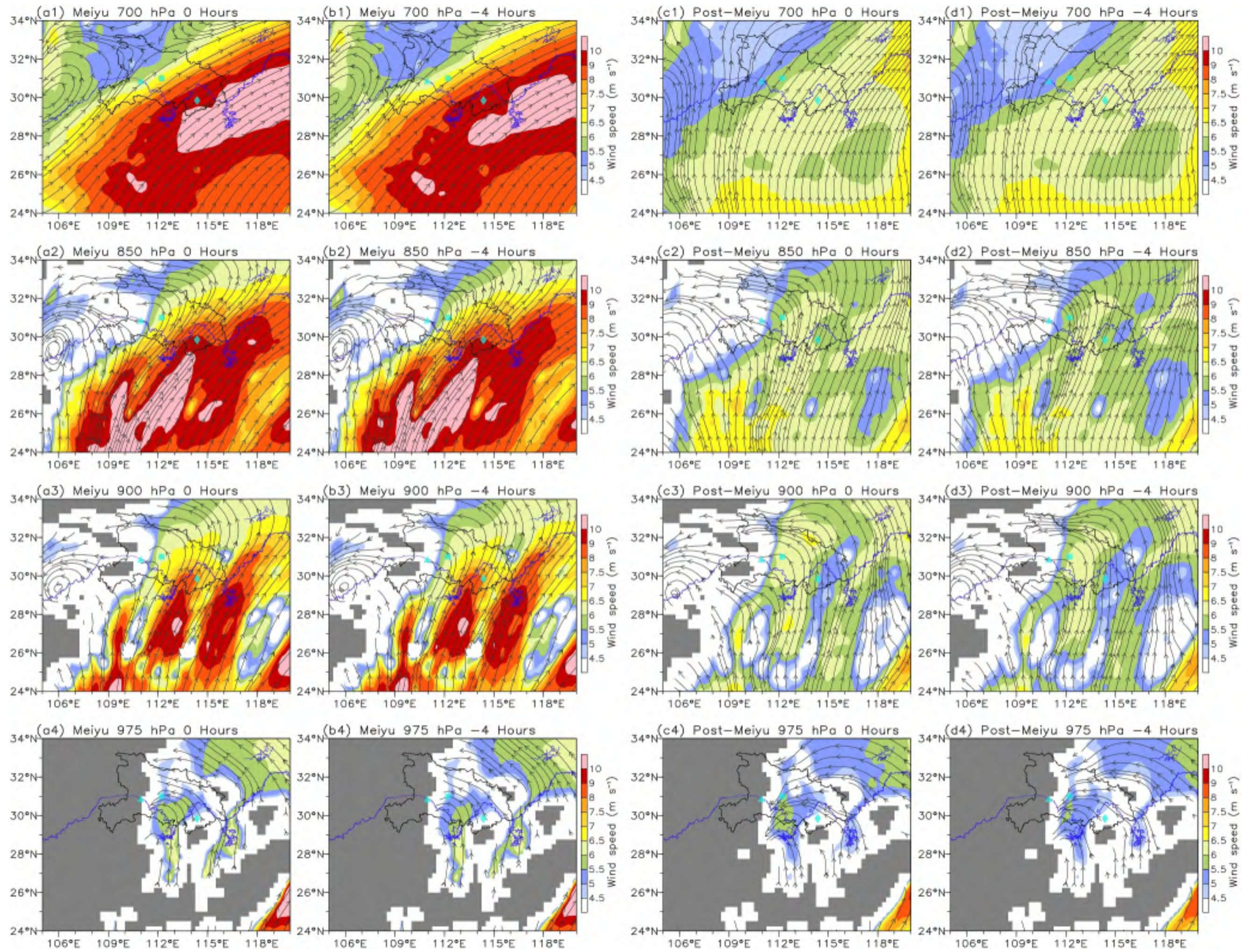

Figure 8. Same as Figure 7, but average during the Meiyu and post-Meiyu periods of 2010–2019.

first. The results show that the vertical wind distributions varied significantly at three stations shortly before FHREs began (Figure 9).

At station XN (Figures 9a1–9a4), wind speeds in the layer below 4 km AGL are highest among the three sites. Winds with speeds ≥ 12 m s^{-1} in the 1–4 km layer range from 29% to 48%, increasing with altitude. One hour before FHRE, southwesterly winds dominate, with directions ranging from 180° to 270°, constituting approximately 58%. Moreover, over 84% of winds exceeding 12 m s^{-1} blow from the southwest. The frequency of winds ≥ 16 m s^{-1} in the 1–2 km layer (Figure 9a2) is 9%, slightly lower than the 11% in the 3–4 km layer (Figure 9a3), but higher than the 6% in the 2–3 km layer (Figure 9a4). These findings indicate the combined influence of synoptic low-level jets and boundary-layer jets on FHREs onset.

Winds at station JM (Figures 9b1–9b4) are notably weaker compared to those at XN, despite prevailing southwesterly winds in the 1–4 km layer. The frequency of wind ≥ 12 m s^{-1} barely exceeds 15%, with 4% (13%) in the 0–2 km (2–4 km) layer. Wind directions in the 1–4 km layer are predominantly concentrated, with more than 66% of winds blowing from 202.5° to 247.5°. Noteworthy is a lower-level northeasterly wind at JM, especially from 315° to 45° in the 0–1 km layer, accounting for 52% (Figure 9b1). About 69% of winds exceeding 8 m s^{-1} are northeasterly jets, potentially stemming from the barrier jet (Markowski & Richardson, 2011) due to the damming of the north-south oriented mountains.

At station ZG, wind occurrences exceeding 8 m s^{-1} are less than 8% (Figures 9c1–9c4), the minimum among the three WPR sites. Winds are predominantly south-southeasterly in the 0–2 km layer (Figures 9c1 and 9c2) and

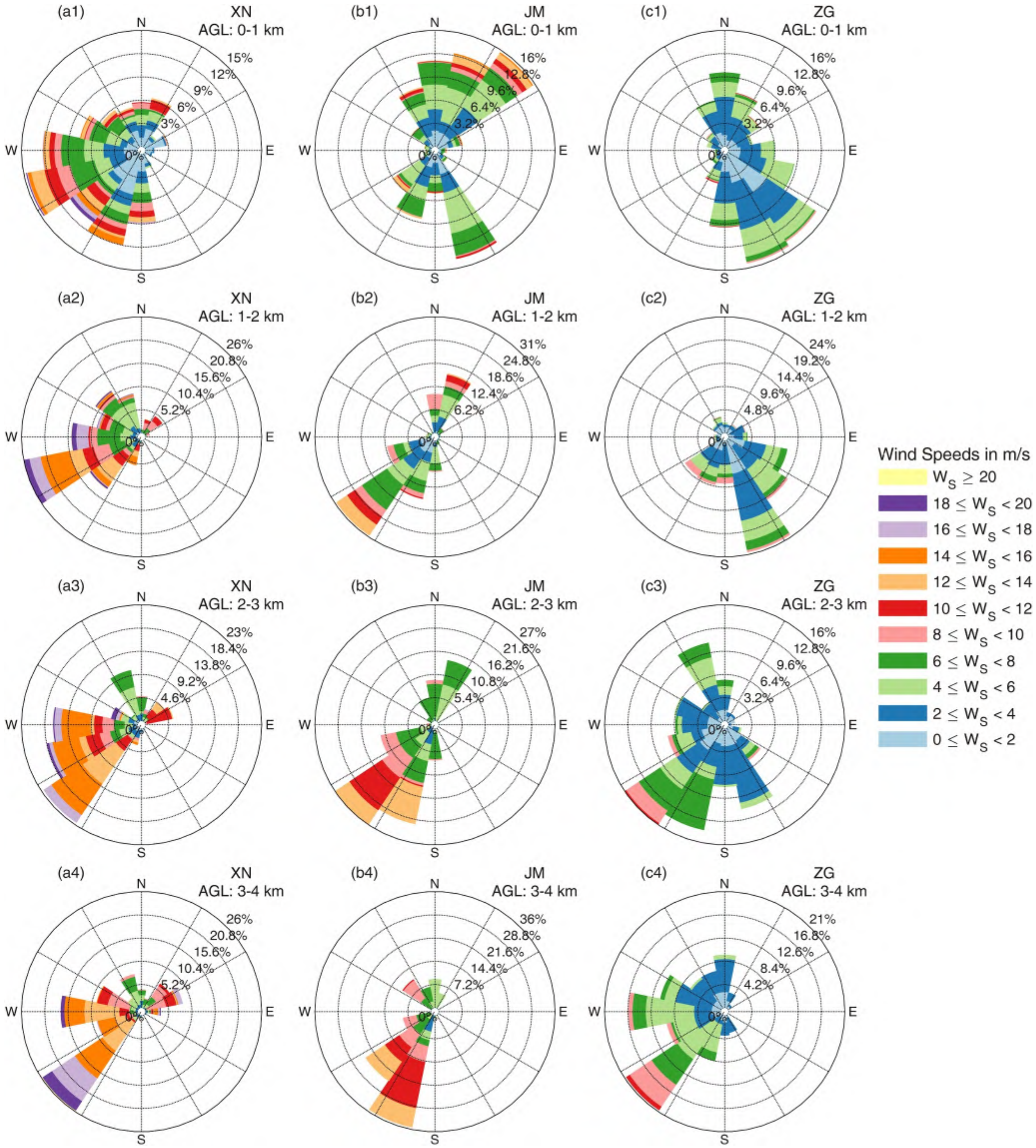

Figure 9. Wind roses at XN, JM, and ZG, within 1 hr before the flash heavy rain events occurring at stations outlined in white in Figure 1, during the summers of 2015–2019. Wind roses are shown for heights of (a1–c1) 0–1 km, (a2–c2) 1–2 km, (a3–c3) 2–3 km, and (a4–c4) 3–4 km above ground level (AGL).

southwesterly in the 2–4 km layer (Figures 9c3 and 9c4). The consistent direction in the deeper layer (0–2 km) suggests the impact of local-scale thermal and dynamic forcings on the wind profile at ZG, influenced by its location in a canyon of the western mountains (Figure 1b).

Although large-scale variations in low-troposphere winds before FHREs are negligible during both the Meiyu and post-Meiyu periods (Figure 8), the 38 FHREs with available WPR observations mainly occurred during these two periods. Excluding the single pre-Meiyu FHRE at station JM, analyses of detailed wind features within hours before FHREs could provide precise insights into the changes in winds and their corresponding timing, potentially improving the accuracy of FHRE warnings.

The great magnitudes of wind consistency within 4–8 hr before summer FHREs below 2 km AGL at these stations (Figures 10a–10c) demonstrate the meaningful indicators for FHREs. In summer (Figure 10a), westerly and southwesterly winds are predominant at station XN within 12 hr before FHREs. Wind speeds notably increase 6 (3) hours before FHREs at altitudes of 1 km (above 1 km AGL). During the Meiyu period (Figure 10d), dominant southwesterly winds are consistently present 12 hr before most FHREs, even 73% of FHREs occur during this period. Accelerated wind speed begins early, around 11 hr (9 hr) before FHREs in the 1–2 km layer (2–4 km layer), with further intensification observed 4 hr prior to FHREs in the boundary layer and lower troposphere simultaneously. It shows sustained wind speed acceleration 5–7 hr before post-Meiyu FHREs above 600 m altitude (Figure 10g). Notably, northerly winds prevail during three out of four FHRE occurrences near station XN (Figure 10g), influenced by landfall typhoons and the compression effect of continental high due to typhoons (figure not shown).

Preceding FHREs at station JM in summer, wind patterns are mainly influenced by those during the Meiyu period (Figures 10b, 10e, and 10h), despite Meiyu FHREs comprising only 56% of total occurrences. During the Meiyu period (Figure 10e), southwesterly winds also dominate at JM with stronger southerly components compared to XN, persisting below 4 km AGL from 6 hr before. Wind speeds increase above 0.5 km AGL during the 6 to 2 hr before FHREs but decrease thereafter. Additionally, winds near the surface shift from southerlies to northerlies approximately 2 hr before FHREs as speed decreases. During the post-Meiyu period (Figure 10h), the low wind consistency (below 0.5) before FHREs indicates various systems conducive to precipitation, with prevalent northerly winds below 800 m AGL and intense wind speeds in the 2–4 km layer 2 hr prior.

At station ZG, wind patterns preceding FHREs exhibit similar during the Meiyu and post-Meiyu periods (Figures 10f and 10i), characterized by prevailing westerly or southwesterly winds above 1.5 km AGL and easterly or northerly winds below. Variations in wind speed before FHREs are negligible compared to other stations, whereas noticeable clockwise wind rotations attributed to thickened southerly winds in the 0.7–2 km layer occur 4–5 hr before.

Respectively, the changes in wind speed, direction, and vertical shear preceding FHREs reveal specific warning features associated with low-level (≤4 km AGL) winds. Changes in the wind speed during the Meiyu period dominate the summer characteristics, exhibiting similar changes, except for reduced speeds in the post-Meiyu period (figure not shown).

Boxplots of wind speeds within 12 hr before summer FHREs (Figures 11a1–11a4) show that 25% exceed 12 m s^{-1}, occurring 4–6 hr before FHREs above 1 km AGL at station XN. These higher speeds in the 1–2 km layers precede those in the 2–3 km layers by 2 hr, indicating that boundary layer jets precede the synoptic low-level jets. Particularly distinctive jet-like wind profiles, with maximum speeds around 1 km AGL, are observed at XN compared to the other stations (figure not shown). Notable acceleration across the entire layer, including increases in the 25th percentiles, medians, and means, is observed 3–4 hr before FHREs. In the final hour prior, wind speeds in the 2–4 km layers experience a significant surge, with approximately 50% of them exceeding 12 m s^{-1}. Wind speeds preceding FHREs at station JM (Figures 11b1–11b4) are lower than XN, with more than 75% below 12 m s^{-1}. Speeds notably increase 5 hr before FHREs but decrease 1 hr prior, except in the 0–1 km layer. At station ZG (Figures 11c1–11c4), 75% of wind speeds are below 8 m s^{-1}, with no evident wind acceleration preceding FHREs. Additionally, changes in wind speed vary inconsistently at different heights.

The changes in wind direction before summer FHREs are depicted by the hourly relative frequency of horizontal wind directions (Figure 12). At station XN (Figures 12a1–12a4), west-southwest components (225°–270°), commonly observed during the Meiyu period, dominate the layer below 4 km AGL 12 hr before FHREs. At higher altitudes, southerly wind (135°–225°) show reduced influence. The frequency of west-southwest winds below 4 km increases to approximately 24%–45% around 4–6 hr prior, preceding the intensification of wind speeds by 1–2 hr (Figures 11a1–11a4). During the post-Meiyu period, a notable shift occurs from predominant

10.1029/2024EA003902

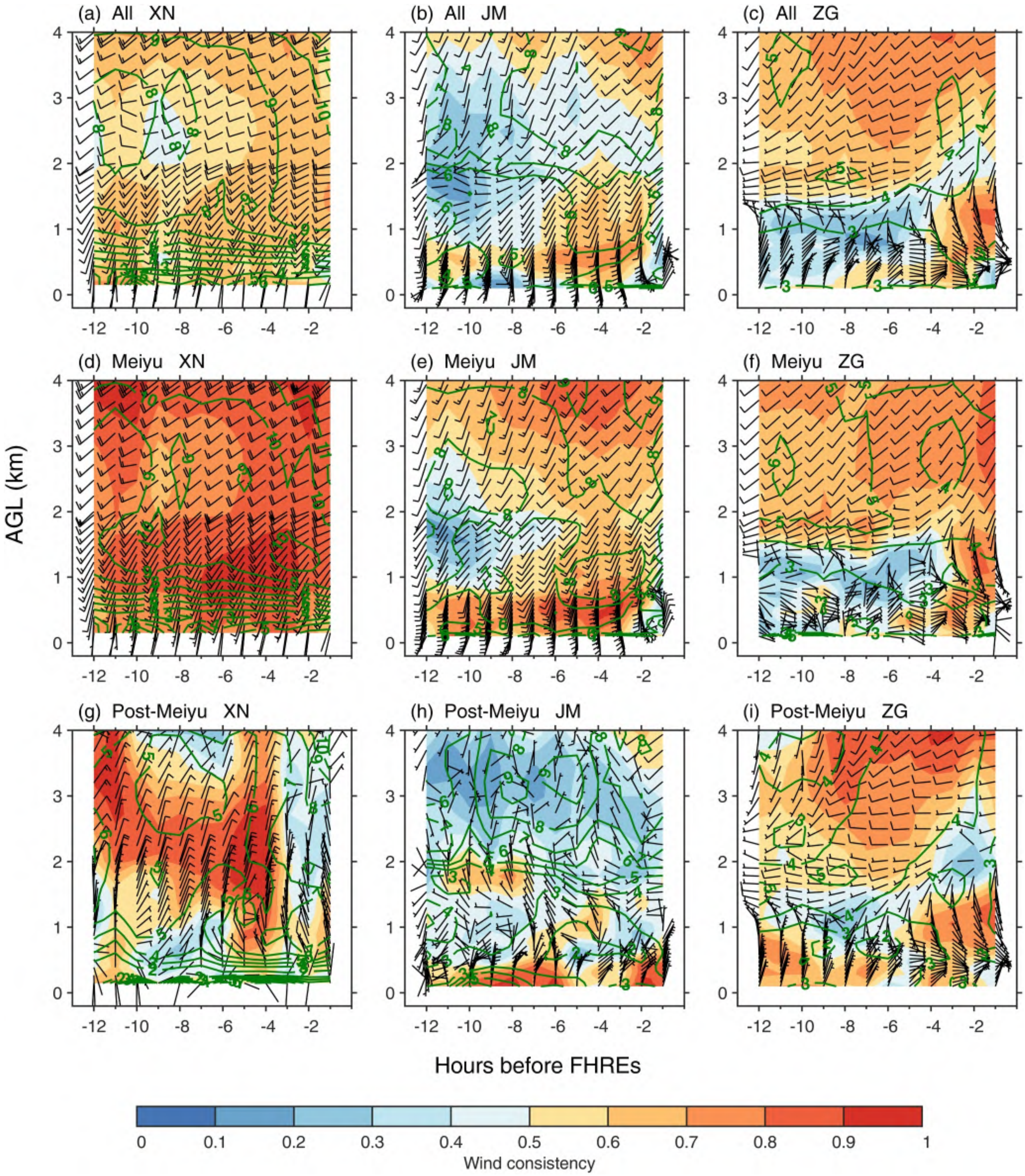

Figure 10. Wind profiles at stations XN, JM, and ZG, within 12 hr before the flash heavy rain events occurring at stations outlined in white in Figure 1, during the (a–c) summers, (d–f) Meiyu, and (g–i) post-Meiyu periods of 2015–2019. The half and full barbs represent averaged vector winds with speeds of 2, and 4 m s^{-1}, respectively. Contours show the average wind speed. Shadings indicate the wind consistency calculated by Equation 3.

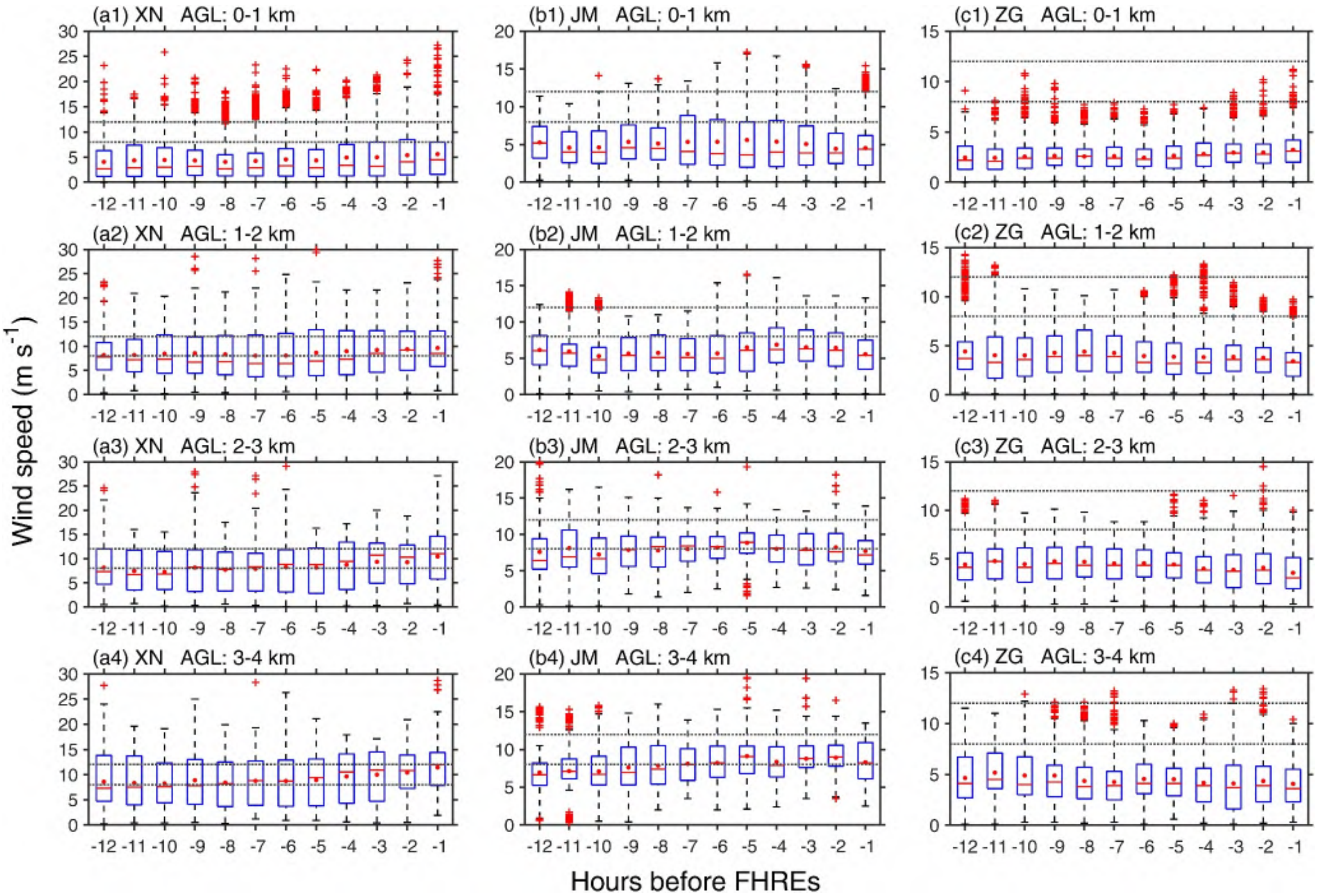

Figure 11. Horizontal wind speeds at stations XN, JM, and ZG within 12 hr before the flash heavy rain events during the summers of 2015–2019 for heights of (a1–c1) 0–1 km, (a2–c2) 1–2 km, (a3–c3) 2–3 km, and (a4–c4) 3–4 km AGL. The red "−" symbol in the box indicates the median, while the red dot represents the mean. Lower and upper gray dotted lines depict horizontal wind speeds of 8 and 12 m s^{-1}, respectively.

northerly winds (Figures 11a1–11a4) to more frequent southwesterly winds approximately 3 hr before (figure not shown). At station JM, southwesterly winds (202.5°–225°) dominate the 1–4 km layer 12 hr before FHREs, particularly during the Meiyu period (Figures 12b2–12b4). Northerly wind components (315°–45°) notably increase in the 0–2 km layer 1–2 hr before FHREs during both Meiyu and post-Meiyu periods (Figures 12b1–12b2), corresponding to a decrease in wind speed (Figures 11b1–11b3). In the 0–1 km layer, northerly components increase to 15%, while southerly components decrease from 25% to 10%. At station ZG, changes in wind direction (Figures 12c1–12c4) are more distinct than changes in wind speed, remaining consistent from the Meiyu to post-Meiyu periods (Figures 10f and 10i). In the 2–4 km layer, westerly winds (270°) prevail, with their frequency decreasing 3–4 hr before FHREs onset (Figures 12c3 and 12c4). Southeasterly winds (112.5°–180°) become more prevalent in the 0–2 km layer approximately 4 hr prior (Figures 12c1 and 12c2), aiding in transporting water vapor from the eastern lowlands.

Vertical wind shear plays a crucial role in initiating and enhancing convections, which can directly cause FHREs. According to Rotunno et al. (1988), the balance of vorticity between low-level ambient wind shear and the cold pool is critical for the initiation of new convective cells. Additionally, the maintenance and enhancement of convective systems rely on achieving an energy equilibrium between strong deep-layer wind shear and convective available potential energy, as noted by Markowski and Richardson (2011). In this study, the shear of horizontal wind is calculated by $|\Delta V| = \sqrt{\left(V_1^2 + V_2^2 - 2V_1V_2\,cosD\right)}$, where V_1 and V_2 represent the horizontal winds at different altitudes and D denotes the difference in wind direction between V_1 and V_2 (M. Hu, 2015).

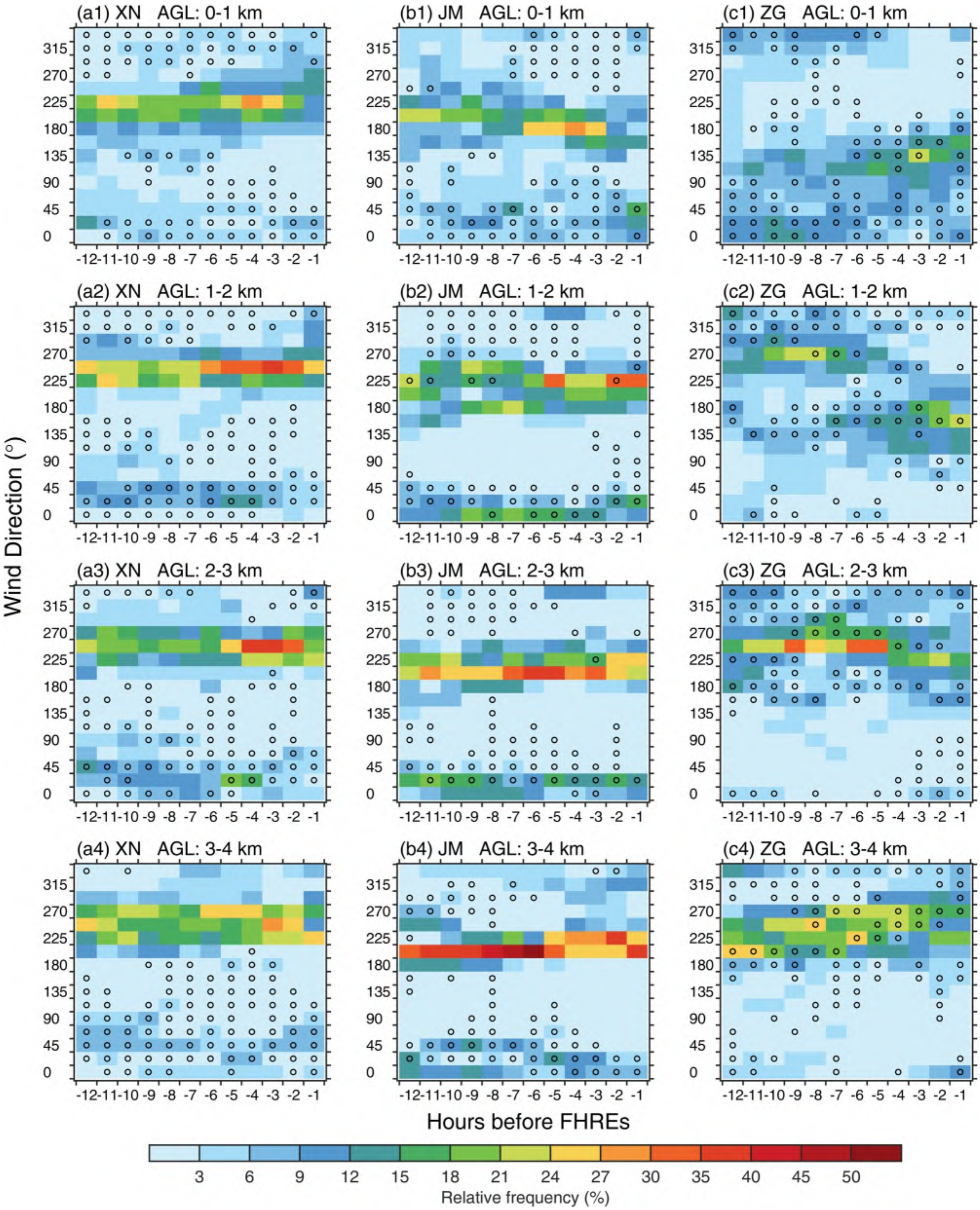

Figure 12. Relative frequency (shading, unit: %) of horizontal wind direction at stations XN, JM, and ZG within 12 hr before the onset of flash heavy rain events during the summers of 2015–2019 for heights of (a1–c1) 0–1 km, (a2–c2) 1–2 km, (a3–c3) 2–3 km, and (a4–c4) 3–4 km AGL. Black circles denote >50% contribution from post-Meiyu periods.

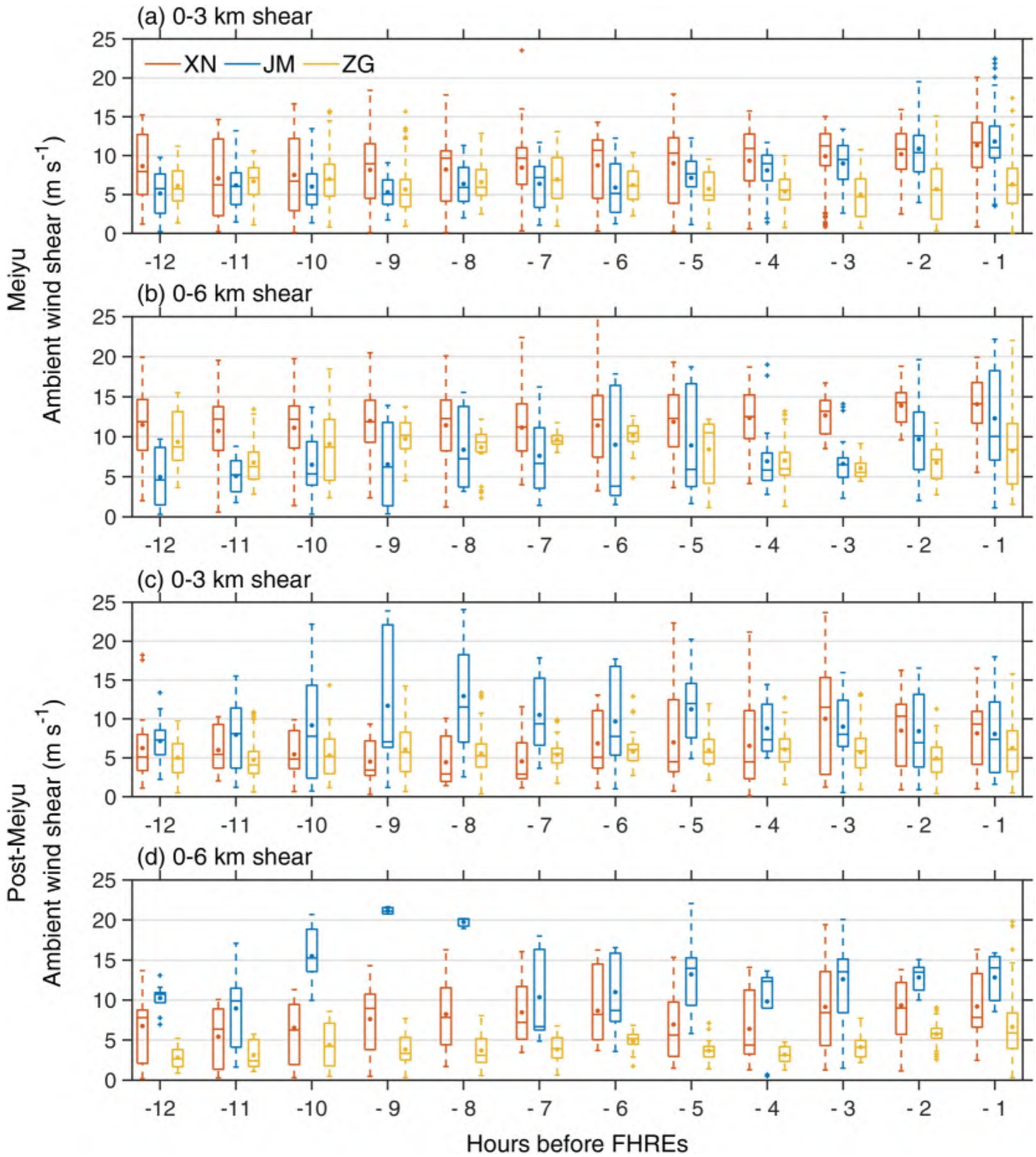

Figure 13. Magnitude of 0–3 km and 0–6 km shear at stations XN, JM, and ZG within 12 hr before the onset of flash heavy rain events during the (a–b) Meiyu and (c–d) post-Meiyu periods of 2015–2019. The "–" symbol in the box indicates the median, while the dot represents the mean.

Consequently, wind shear variations preceding FHREs (Figure 13) are closely associated with significant changes in wind speed and direction (Figures 11 and 12). At station XN, both the 0–3 and 0–6 km shears exhibit a similar notable increase starting from 3 hr before FHRE, with higher magnitudes during the Meiyu period than the post-Meiyu period. The 25th percentiles of shears consistently enhance 3 hr before the FHREs in the Meiyu period, while medians increase in the post-Meiyu period. Peaks are observed within 1 hr before FHREs in the Meiyu period and 3 hr before in the post-Meiyu period. At station JM during the Meiyu period, 75% of 0–3 km shears exceed 5 m s^{-1} beginning 5 hr before FHREs (Figure 13a), while 0–6 km shears sharply increase 2 hr prior (Figure 13b). Comparatively, variations in wind shears are less pronounced in the post-Meiyu periods, despite higher medians for both types of shears. Station ZG experiences predominantly wind shears below 10 m s^{-1} in summer, the lowest among the three stations. Within 6 hr before FHREs, median values for both 0–3 and 0–6 km shears initially decrease followed by a subsequent rise. The weakest shears occur 3 hr before the FHREs during

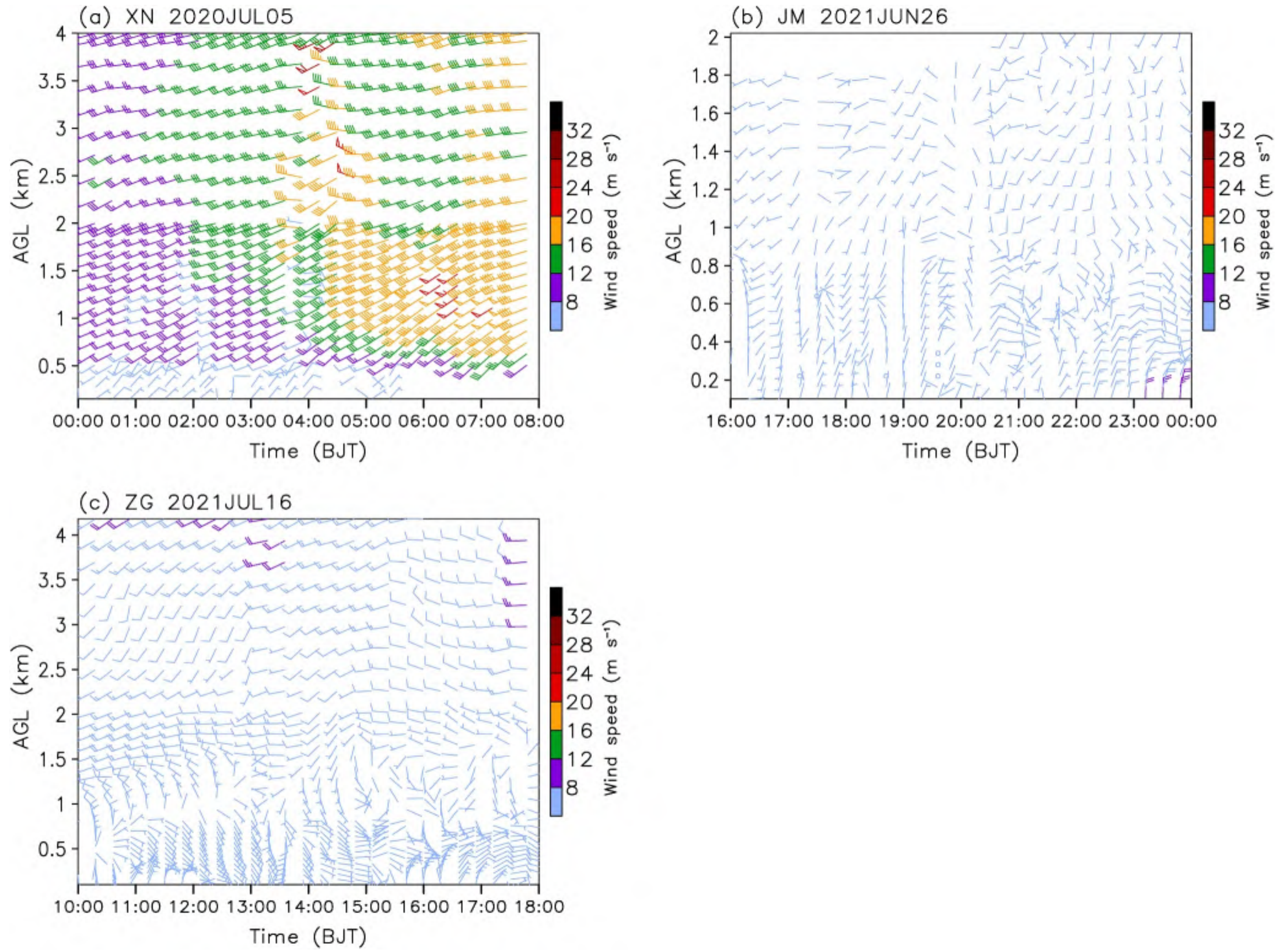

Figure 14. Time–height cross sections of wind vectors at the stations (a) XN, (b) JM, and (c) ZG within 8 hr before the occurrence of flash heavy rain event cases. Colors show the magnitude of horizontal wind speed (unit: m s^{-1}); half, full barbs, and pennants denote wind speeds of 2, 4, and 20 m s^{-1}, respectively.

the Meiyu period. However, during the post-Meiyu period, the weakest 0–3 km (0–6 km) shear appears 2 hr (4 hr) prior.

To evaluate the applicability of the statistical characteristics in warning of specific FHRE cases, the vertical wind profiles within 8 hr preceding the FHRE occurring in the summers of 2020–2021 near the stations XN, JM, and ZG are shown in Figure 14. At station XN (Figure 14a), westerly winds above 2 km AGL prevailed before the FHRE with speeds exceeding 16 m s^{-1} starting 1 hr prior. In contrast, wind speeds below 2 km AGL gradually intensified, surpassing 16 m s^{-1} 4 hr before the FHRE. Concurrently, the southerly component of the wind strengthened, and wind directions exhibited a clockwise rotation with height, indicating that both speed and directional shear make the wind shear favorable for the initiation and maintenance of heavy rain. At station JM (Figure 14b), weak southerly winds dominated above 1 km before the FHRE, with significant wind disturbances appearing below 1 km AGL starting 6 hr before. Northerly winds emerged 2 hr prior and further intensified to exceeding 8 m s^{-1} as the FHRE approached, accompanied by a clockwise rotation of wind with altitude. At station ZG (Figure 14c), weak westerly and easterly winds prevailed above 2 km and below 0.7 km AGL, respectively. Southerly wind components increased significantly in the 0.7–2 km layer 4 hr before the FHRE, and this layer deepened as the FHRE approached. All these changes in the winds before rainfall align with the results obtained from the statistical analyses, indicating that the previously identified wind profile features could be used to warn of the FHREs over the MYRB.

4. Conclusions and Discussion

The spatiotemporal distributions of FHREs in the middle reaches of the Yangtze River basin (MYRB) during the summers (June–August) of 2010–2019 were analyzed using hourly rainfall observations from a dense network of surface rain gauges. ERA5 reanalysis data were employed to investigate the prevailing wind patterns preceding FHREs. Furthermore, detailed wind profiles below 4 km above ground level (AGL), conducive to FHRE warnings, were elucidated through WPR observations at three representative sites across the MYRB: station XN (southeastern MYRB), station JM (western mountains front), and station ZG (western mountainous area) during the summers of 2015–2019.

The results indicate that FHREs over the MYRB predominantly occur during the Meiyu period, which extends from mid-June to early July and represents only 29% of summertime days. These Meiyu events are characterized by their high frequency and significant contribution to total precipitations. Moreover, Meiyu FHREs last longer and occur more often during the late night to early morning hours. Spatially, the increase in FHRE frequency from the northwest to the southeast within the MYRB, along with the higher frequencies observed in the topographic transition areas, is shaped by the northward-advancing summer monsoon and the complex mesoscale terrain.

Over the MYRB, strong southwesterly winds in the lower troposphere and easterly winds in the boundary layer facilitate significant moisture convergence 4 hr before FHREs. This moisture convergence intensified and deepened during the Meiyu period. Moreover, 12 hr before summer FHREs, low-level prevailing horizontal winds are strengthening from the western to eastern MYRB, accompanied by a less pronounced clockwise rotation with altitude, shifting from easterly to westerly winds. These prevailing wind patterns are closely associated with the frequent synoptic low-level jets, boundary-layer jets, and quasi-steady mesoscale cyclonic wind shear. The surge in southerly winds and the enhancement of cyclonic wind shear hours before FHREs are particularly notable during the pre-Meiyu period.

The wind profiles observed 12 hr before summer FHREs indicate prevalent westerly and southwesterly winds over the MYRB above 1–2 km AGL. During both the Meiyu and post-Meiyu periods, significant changes in wind speeds occur predominantly over the southeastern MYRB, whereas noticeable variations in wind directions are observed over the western mountainous area. Over the southeastern MYRB, west-southwest wind speeds begin to rise significantly 3–4 hr before FHREs, with increases in southerly components starting 2 hr earlier. The wind speeds peak in the last hour before FHREs, with around 50% of wind speeds above 2 km AGL exceeding 12 m s^{-1}. Notably, wind speeds in the 0.8–2 km layer intensify within 4–6 hr before FHREs, earlier than those in the 2–4 km layer. In front of the western mountains, prevailing southwesterly winds in the 1–4 km layer accelerate 5 hr before the FHREs but significantly weaken in the final hour prior. Meanwhile, southerly winds in the 0–1 km layer shift noticeably to northerly within the final hour prior, accompanied by a slight increase in speed. This distinct shift and acceleration in the 0–1 km layer persist into the post-Meiyu period, despite northerly winds above 1 km AGL. Over the western mountainous area, wind speeds remain consistently low before FHREs, with minimal variations. Four hours before FHREs, as southerly components intensify and extend vertically up to 2 km AGL, there is a noticeable clockwise rotation in wind direction with altitude, shifting from easterly to westerly. Moreover, these accelerations and veering of wind before FHREs over the MYRB contribute significantly to vertical wind shears, especially the 0–3 km shears.

This study focuses on significant changes in horizontal winds over the MYRB preceding FHREs. However, detailed variations in meso-β and meso-γ scale momentum factors, including convergence, shear, vortices, and gravity waves might have been overlooked due to the single-site observations without a WPR network (Liu et al., 2020). Therefore, more comprehensive studies on the dynamic factors in the lower troposphere preceding the FHREs can be conducted once a dense wind profile network in the MYRB is established in the future. Enhancing the accuracy of these warning signals would not only deepen our understanding of the mechanisms triggering heavy rain but also improve flash heavy rain forecasting and early warnings (Wang, Chen, & Chen, 2022).

Data Availability Statement

The global topography data set is obtained from NOAA National Centers for Environmental Information (2022). The ERA5 reanalysis data is available at Hersbach et al. (2023). The surface rainfall and WPR observations are obtained from China's National Meteorological Data Center (CMA, 2023).

Acknowledgments
This study was funded by the National Natural Science Foundation of China (Grant 42230612, 42475018), the Natural Science Foundation of Hubei Province (2023AFD102, 2023AFD093, 2023AFD092), the Joint Research Project for Meteorological Capacity Improvement (23NLTSQ004), the Open Fund Project for Heavy Rain (BYKJ2024M01), and the China Meteorological Administration Xiong'an Atmospheric Boundary Layer Key Laboratory (2023LABL-B10). Thanks are extended to Leng Liang, the associate research fellow at the Institute of Heavy Rain, CMA, for assistance with the application of the WPR data.

References

Benjamin, S. G., Schwartz, B. E., Szoke, E. J., & Koch, S. E. (2004). The value of wind profiler data in US weather forecasting. *Bulletin of the American Meteorological Society*, *85*(12), 1871–1886. https://doi.org/10.1175/BAMS-85-12-1871

Brooks, H. E., & Stensrud, D. J. (2000). Climatology of heavy rain events in the United States from hourly precipitation observations. *Monthly Weather Review*, *128*(4), 1194–1201. https://doi.org/10.1175/1520-0493(2000)128%3C1194:COHREI%3E2.0.CO;2

Chen, Y., Wang, X., Huang, L., & Luo, Y. (2021). Spatial and temporal characteristics of abrupt heavy rainfall events over Southwest China during 1981–2017. *International Journal of Climatology*, *41*(5), 3286–3299. https://doi.org/10.1002/joc.7019

CMA. (2023). Surface and upper-air observations in China [Dataset]. *China Meteorological Administration*. http://data.cma.cn

Coleman, T. A., & Knupp, K. R. (2011). Radiometer and profiler analysis of the effects of a bore and a solitary wave on the stability of the nocturnal boundary layer. *Monthly Weather Review*, *139*(1), 211–223. https://doi.org/10.1175/2010MWR3376.1

Cui, C., Wan, R., & Wang, B. (2011). A mesoscale heavy rainfall observing system in the middle reach of Yangtze River and its preliminary applications. In *Advances in geosciences* (Vol. 23, pp. 103–119). https://doi.org/10.1142/9789814355339_0009

Cui, C., Zhou, W., Yang, H., Wang, X., Deng, Y., Wang, X., et al. (2023). Analysis of the characteristics of the low-level jets in the middle reaches of the Yangtze River during the Mei-yu season. *Advances in Atmospheric Sciences*, *40*(4), 711–724. https://doi.org/10.1007/s00376-022-2107-1

Deng, X., He, D., Zhang, G., Zhu, S., Dai, R., Jin, X., et al. (2022). Comparison of horizontal wind observed by wind profiler radars with ERA5 reanalysis data in Anhui, China. *Theoretical and Applied Climatology*, *150*(3), 1745–1760. https://doi.org/10.1007/s00704-022-04247-6

Doswell, C. A., III, Brooks, H. E., & Maddox, R. A. (1996). Flash flood forecasting: An ingredients-based methodology. *Weather and Forecasting*, *11*(4), 560–581. https://doi.org/10.1175/1520-0434(1996)011%3C0560:FFFAIB%3E2.0.CO;2

Du, Y., & Chen, G. (2019). Heavy rainfall associated with double low-level jets over southern China. Part II: Convection initiation. *Monthly Weather Review*, *147*(2), 543–565. https://doi.org/10.1175/MWR-D-18-0102.1

Du, Y., Zhang, Q., Chen, Y. L., Zhao, Y., & Wang, X. (2014). Numerical simulations of spatial distributions and diurnal variations of low-level jets in China during early summer. *Journal of Climate*, *27*(15), 5747–5767. https://doi.org/10.1175/JCLI-D-13-00571.1

Feng, X., Liu, C., Fan, G., Liu, X., & Feng, C. (2016). Climatology and structures of southwest vortices in the NCEP climate forecast system reanalysis. *Journal of Climate*, *29*(21), 7675–7701. https://doi.org/10.1175/JCLI-D-15-0813.1

Fu, S. M., Tang, H., Sun, J. H., Zhao, T. B., & Li, W. L. (2022). 'Historical rankings and vortices' activities of the extreme Mei-yu seasons: Contrast 2020 to previous Mei-yu seasons. *Geophysical Research Letters*, *49*(2), e2021GL096590. https://doi.org/10.1029/2021GL096590

Gao, Z., Ming, Y., & You, Z. (2021). Analysis on wind profiling radar data of a rainstorm at Lin'an. In *2021 CIE international conference on radar (radar)* (pp. 2417–2422). IEEE. https://doi.org/10.1109/Radar53847.2021.10028059

Garcia-Benadi, A., Bech, J., Udina, M., Campistron, B., & Paci, A. (2022). Multiple characteristics of precipitation inferred from wind profiler radar Doppler spectra. *Remote Sensing*, *14*(19), 5023. https://doi.org/10.3390/rs14195023

Grubbs, F. E. (1969). Procedures for detecting outlying observations in samples. *Technometrics*, *11*(1), 1–21. https://doi.org/10.1080/00401706.1969.10490657

Guo, X., Guo, J., Zhang, D. L., & Yun, Y. (2023). Vertical divergence profiles as detected by two wind profiler mesonets over east China: Implications for nowcasting convective storms. *Quarterly Journal of the Royal Meteorological Society*, *149*(754), 1–21. https://doi.org/10.1002/qj.4474

Hersbach, H., Bell, B., Berrisford, P., Biavati, G., Horanyi, A., Munoz Sabater, J., et al. (2023). ERA5 hourly data on pressure levels from 1940 to present [Dataset]. *Copernicus Climate Change Service (C3S) Climate Data Store (CDS)*. https://doi.org/10.24381/cds.bd0915c6

Hu, B., Cui, C., & Fang, C. (2001). Causes of a two-day successively extremely heavy rain along the changjiang valley in the eastern Hubei Province during 21∼22 July 1998. *Chinese Journal of Atmospheric Sciences*, *25*(4), 479–491. (in Chinese). https://doi.org/10.3878/j.issn.1006-9895.2001.04.05

Hu, M. (2015). *Wind profiler radar detection and application*. China Meteorological Press. 18pp, 151pp, 151pp (in Chinese).

Huang, T. T., Fu, S. M., Wang, Z. G., Zhao, S., Sun, J. H., Zhang, Y., & Wang, S. H. (2024). A case study on the rainstorm-producing mesoscale vortices in central-eastern China. *Journal of Geophysical Research: Atmospheres*, *129*(5), e2023JD039573. https://doi.org/10.1029/2023JD039573

Larsen, M. F., & Röttger, J. (1982). VHF and UHF Doppler radars as tools for synoptic research. *Bulletin of the American Meteorological Society*, *63*(9), 996–1008. https://doi.org/10.1175/1520-0477(1982)063%3C0996:VAUDRA%3E2.0.CO;2

Leng, L., Zhou, L., Xiao, Y., Wang, J., & Wu, D. (2021). Analysis of temporal and spatial distribution characteristics of flash heavy rain in Hubei Province based on minute rain gauge data. *Torrential Rain and Disasters*, *40*(1), 61–68. (in Chinese). https://doi.org/10.3969/j.issn.1004-9045.2021.01.008

Liu, B., Guo, J., Gong, W., Shi, L., Zhang, Y., & Ma, Y. (2020). Characteristics and performance of wind profiles as observed by the radar wind profiler network of China. *Atmospheric Measurement Techniques*, *13*(8), 4589–4600. https://doi.org/10.5194/amt-13-4589-2020

Luo, Y., Wu, M., Ren, F., Li, J., & Wong, W. K. (2016). Synoptic situations of extreme hourly precipitation over China. *Journal of Climate*, *29*(24), 8703–8719. https://doi.org/10.1175/JCLI-D-16-0057.1

Markowski, P., & Richardson, Y. (2011). *Mesoscale meteorology in midlatitudes*. John Wiley & Sons. 41-58pp, 350-351pp, 58-61pp, 161pp, 202-203pp. https://doi.org/10.1002/9780470682104

May, P. T., & Wilczak, J. M. (1993). Diurnal and seasonal variations of boundary-layer structure observed with a radar wind profiler and RASS. *Monthly Weather Review*, *121*(3), 673–682. https://doi.org/10.1175/1520-0493(1993)121%3C0673:DASVOB%3E2.0.CO;2

Neiman, P. J., May, P. T., & Shapiro, M. A. (1992). Radio acoustic sounding system (RASS) and wind profiler observations of lower-and midtropospheric weather systems. *Monthly Weather Review*, *120*(10), 2298–2313. https://doi.org/10.1175/1520-0493(1992)120%3C2298:RASSAW%3E2.0.CO;2

NOAA National Centers for Environmental Information. (2022). ETOPO 2022 15 arc-second global relief model [Dataset]. *NOAA National Centers for Environmental Information*. https://doi.org/10.25921/fd45-gt74

Rotunno, R., Klemp, J. B., & Weisman, M. L. (1988). A theory for strong, long-lived squall lines. *Journal of the Atmospheric Sciences*, *45*(3), 463–485. https://doi.org/10.1175/1520-0469(1988)045%3C0463:ATFSLL%3E2.0.CO;2

Shapiro, M. A., Hample, T., & Van De Kamp, D. W. (1984). Radar wind profiler observations of fronts and jet streams. *Monthly Weather Review*, *112*(6), 1263–1266. https://doi.org/10.1175/1520-0493(1984)112%3C1263:RWPOOF%3E2.0.CO;2

Stewart, J. Q., Whiteman, C. D., Steenburgh, W. J., & Bian, X. (2002). A climatological study of thermally driven wind systems of the US Intermountain West. *Bulletin of the American Meteorological Society*, *83*(5), 699–708. https://doi.org/10.1175/1520-0477(2002)083<0699:ACSOTD>2.3.CO;2

Strauch, R. G., Weber, B. L., Frisch, A. S., Little, C. G., Merritt, D. A., Moran, K. P., & Welsh, D. C. (1987). The precision and relative accuracy of profiler wind measurements. *Journal of Atmospheric and Oceanic Technology*, *4*(4), 563–571. https://doi.org/10.1175/1520-0426(1987)004%3C0563:TPARAO%3E2.0.CO;2

Sun, J., Xiaoling, Z., Linlin, Q., & Sixiong, Z. (2005). An analysis of a meso-β system in a Mei-yu front using the intensive observation data during CHeRES 2002. *Advances in Atmospheric Sciences*, *22*(2), 278–289. https://doi.org/10.1007/BF02918517

Sun, J., & Zhang, F. (2012). Impacts of mountain–plains solenoid on diurnal variations of rainfalls along the mei-yu front over the east China plains. *Monthly Weather Review*, *140*(2), 379–397. https://doi.org/10.1175/MWR-D-11-00041.1

Tao, S. (1980). *Heavy rainfalls in China*. Science Press. 13-23pp, 91-115pp, 51-56pp, (in Chinese).

Tao, S. Y., & Ding, Y. H. (1981). Observational evidence of the influence of the Qinghai-Xizang (Tibet) Plateau on the occurrence of heavy rain and severe convective storms in China. *Bulletin of the American Meteorological Society*, *62*(1), 23–30. https://doi.org/10.1175/1520-0477(1981)062%3C0023:OEOTIO%3E2.0.CO;2

Wang, C., Chen, M., & Chen, Y. (2022). Impact of combined assimilation of wind profiler and Doppler radar data on a convective-scale cycling forecasting system. *Monthly Weather Review*, *150*(2), 431–450. https://doi.org/10.1175/MWR-D-20-0383.1

Wang, J., Li, Z., Wang, X., Wang, X., & Cui, C. (2019). Temporal and spatial distribution characteristics of flash heavy rain in Henan during rainy season. *Torrential Rain and Disasters*, *38*(2), 152–160. (in Chinese). https://doi.org/10.3969/j.issn.1004-9045.2019.02.007

Wang, X., Zhou, R., Deng, Y., Cui, C., Hu, Y., Wang, J., & Liu, H. (2022). Symbiotic relationship between Mei-yu rainfall and the morphology of Mei-Yu Front. *Journal of Hydrometeorology*, *23*(1), 87–100. https://doi.org/10.1175/JHM-D-21-0068.1

Weber, B. L., Wuertz, D. B., Strauch, R. G., Merritt, D. A., Moran, K. P., Law, D. C., et al. (1990). Preliminary evaluation of the first NOAA demonstration network wind profiler. *Journal of Atmospheric and Oceanic Technology*, *7*(6), 909–918. https://doi.org/10.1175/1520-0426(1990)007%3C0909:PEOTFN%3E2.0.CO;2

Wuertz, D. B., Weber, B. L., Strauch, R. G., Frisch, A. S., Little, C. G., Merritt, D. A., et al. (1988). Effects of precipitation on UHF wind profiler measurements. *Journal of Atmospheric and Oceanic Technology*, *5*(3), 450–465. https://doi.org/10.1175/1520-0426(1988)005%3C0450:EOPOUW%3E2.0.CO;2

Xue, M., Luo, X., Zhu, K., Sun, Z., & Fei, J. (2018). The controlling role of boundary layer inertial oscillations in Meiyu frontal precipitation and its diurnal cycles over China. *Journal of Geophysical Research: Atmospheres*, *123*(10), 5090–5115. https://doi.org/10.1029/2018JD028368

Yang, R., Zhang, Y., Sun, J., & Li, J. (2020). The comparison of statistical features and synoptic circulations between the eastward-propagating and quasi-stationary MCSs during the warm season around the second-step terrain along the middle reaches of the Yangtze River. *Science China Earth Sciences*, *63*(8), 1209–1222. https://doi.org/10.1007/s11430-018-9385-3

Yu, R., Xu, Y., Zhou, T., & Li, J. (2007). Relation between rainfall duration and diurnal variation in the warm season precipitation over central eastern China. *Geophysical Research Letters*, *34*(13), L13703. https://doi.org/10.1029/2007GL030315

Yu, X. (2013). Nowcasting thinking and method of flash heavy rain. *Torrential Rain and Disasters*, *32*(3), 202–209. (in Chinese). https://doi.org/10.3969/j.issn.1004-9045.2013.03.002

Zhang, D. L., Lin, Y., Zhao, P., Yu, X., Wang, S., Kang, H., & Ding, Y. (2013). The Beijing extreme rainfall of 21 July 2012: "Right results" but for wrong reasons. *Geophysical Research Letters*, *40*(7), 1426–1431. https://doi.org/10.1002/grl.50304

Zhang, H., & Zhai, P. (2011). Temporal and spatial characteristics of extreme hourly precipitation over eastern China in the warm season. *Advances in Atmospheric Sciences*, *28*(5), 1177–1183. https://doi.org/10.1007/s00376-011-0020-0

Zhang, Q., Li, R., Sun, J., Lu, F., Xu, J., & Zhang, F. (2023). A review of research on the record-breaking precipitation event in Henan Province, China, July 2021. *Advances in Atmospheric Sciences*, *40*(8), 1485–1500. https://doi.org/10.1007/s00376-023-2360-y

Zheng, L., Sun, J., Zhang, X., & Liu, C. (2013). Organizational modes of mesoscale convective systems over central East China. *Weather and Forecasting*, *28*(5), 1081–1098. https://doi.org/10.1175/WAF-D-12-00088.1

Zhong, S., Whiteman, C. D., & Bian, X. (2004). Diurnal evolution of three-dimensional wind and temperature structure in California's Central Valley. *Journal of Applied Meteorology*, *43*(11), 1679–1699. https://doi.org/10.1175/JAM2154.1